

Transcription initiation at a consensus bacterial promoter proceeds via a “bind-unwind-load-and-lock” mechanism

Abhishek Mazumder¹, Richard H Ebright², and Achillefs N Kapanidis¹

¹Biological Physics Research Group, Clarendon Laboratory, Department of Physics, University of Oxford, Oxford, UK

²Waksman Institute and Department of Chemistry, Rutgers University, Piscataway NJ 08854, USA

Correspondence: abhishek.mazumder@physics.ox.ac.uk; kapanidis@physics.ox.ac.uk

Abstract:

Transcription initiation starts with unwinding of promoter DNA by RNA polymerase (RNAP) to form a catalytically competent RNAP-promoter complex (RP_o). Despite extensive study, the mechanism of promoter unwinding has remained unclear, in part due to the transient nature of intermediates on path to RP_o. Here, using single-molecule unwinding-induced fluorescence enhancement to monitor promoter unwinding, and single-molecule fluorescence resonance energy transfer to monitor RNAP clamp conformation, we analyze RP_o formation at a consensus bacterial core promoter. We find that the RNAP clamp is closed during promoter binding, remains closed during promoter unwinding, and then closes further, locking the unwound DNA in the RNAP active-centre cleft. Our work defines a new, “bind-unwind-load-and-lock,” model for the series of conformational changes occurring during promoter unwinding at a consensus bacterial promoter and provides the tools needed to examine the process in other organisms and at other promoters.

Introduction

Transcription initiation is the first and most highly regulated step in gene expression (1,2). During transcription initiation, RNA polymerase (RNAP), together with the transcription initiation factor σ , unwinds ~13 bp of promoter DNA to form a "transcription bubble," and places the template-strand ssDNA of the unwound transcription bubble in contact with the RNAP active center, yielding a catalytically competent RNAP-promoter transcription-initiation complex (RP_O; 1). High-resolution structures of RP_O define the contacts that RNAP and σ make with promoter DNA, as well as the conformation and interactions of unwound template-strand ssDNA engaging the RNAP active center (3-5). Structural and biochemical experiments suggest that transcription-bubble formation is initiated by unwinding the DNA base pair at the upstream end of the transcription bubble--breaking the base pair, and unstacking and flipping the non-template-strand base of the broken base pair, and inserting the unstacked and flipped non-template strand base into a protein pocket of σ --followed by propagation of the unwinding in a downstream direction (1,2,5,6). However, the mechanism by which DNA is unwound and loaded into the RNAP active-center cleft has remained controversial (reviewed in 1). In crystal structures of RNAP- σ holoenzyme, the RNAP active-center cleft is too narrow to accommodate double-stranded DNA (<20 Å), and σ obstructs access of double-stranded DNA to the RNAP active-center cleft (7-10). As a result, there is no unobstructed path by which double-stranded DNA can access the RNAP active-center cleft in RNAP holoenzyme (7-12). Accordingly, it has remained unclear where, when, and how promoter DNA is unwound and loaded into the RNAP active-center cleft.

To address these questions, two classes of models have been proposed. One class of models, termed "load-unwind" models, propose that: (i) the RNAP active-center cleft opens, through the swinging outward of one wall, termed the "clamp," of the active-center cleft, allowing loading of promoter DNA into the active-center cleft as double-stranded DNA; (ii) promoter DNA unwinds inside the active-center cleft; and (iii) the active-center cleft closes, through the swinging inward of the clamp, during or after DNA unwinding (1-2,7-9,11,13-14). The other class of models, termed "unwind-load" models, proposes that: (i) promoter DNA unwinds outside the RNAP active-center cleft, and (ii)

unwound promoter DNA loads into the active-center cleft as single-stranded DNA (1,10). Some versions of the unwind-load model postulate that opening and closing of the RNAP clamp is required for DNA unwinding and DNA loading to occur (15,16). Other versions of the unwind-load model postulate that opening and closing motions of the RNAP clamp is not required for DNA unwinding and DNA loading (17).

Some previous results have been interpreted as supporting *load-unwind* models, including results from static DNA footprinting of trapped putative on-pathway intermediates in formation of RPo, suggesting the presence of double-stranded DNA inside the active-center cleft (18-21), results from kinetic DNA footprinting suggesting the existence of on-pathway intermediates having double-stranded DNA inside the active-center cleft (22), fluorescence resonance energy transfer (FRET) results showing clamp opening and closing in RNAP and in trapped putative on-pathway intermediates in formation of RPo (14,23-25), functional correlations between inhibition of clamp opening and closing with inhibition of formation of RPo (14,23-24), and crystal and cryo-EM structures of trapped putative on-pathway intermediates in formation of RPo having double-stranded DNA inside an open active-center cleft (26).

Other previous results have been interpreted as supporting *unwind-load* models, including time-resolved footprinting experiments suggesting that promoter unwinding occurs outside the active-center cleft and precedes rate-limiting conformational changes in RNAP (27), and cryo-EM structures of trapped putative on-pathway intermediates in formation of RPo containing partly unwound DNA inside a closed active-center cleft (17).

However, the previous results either have relied on analysis of artificially trapped complexes that have not been firmly established to correspond to *bona fide* on-pathway intermediates, or have relied on analysis of ensemble kinetics for which the identities and orders of appearance of intermediates have not been firmly established (14,18-27). Moreover, the previous results have been complicated by differences in the species source of the RNAP analyzed, differences in the σ factors analyzed, and differences in the promoter sequences analyzed (14,18-27). Here, we report the use of single-molecule

kinetic studies to define the pathway of DNA unwinding and DNA loading, without the assumptions that complicate analysis of artificially trapped complexes, and without the heterogeneity, population averaging, and time averaging that complicate analysis of ensemble kinetics. We used single-molecule promoter unwinding-induced fluorescence enhancement (smUIFE) to monitor DNA unwinding in solution in real time during formation of RPo, and we used single-molecule fluorescence resonance energy transfer (smFRET) to monitor opening and closing of the RNAP clamp in solution in real time during formation of RPo. In all experiments, we analyzed *Escherichia coli* RNAP σ^{70} holoenzyme at a consensus bacterial core promoter, comprising a consensus -35 element, a consensus -10 element, and a consensus -35/-10 spacer.

Results

Single-molecule unwinding-induced fluorescence enhancement (smUIFE)

Previous work indicates that a promoter derivative having the fluorescent probe Cy3 site-specifically incorporated in the transcription-bubble region exhibits a ~2-fold increase in fluorescence emission intensity upon promoter unwinding during RPo formation and exhibits a ~2-fold decrease in fluorescence emission intensity upon promoter rewinding during promoter escape (15,28,29). These changes in fluorescence emission intensity provide a powerful approach to monitor promoter unwinding and rewinding in solution during transcription initiation (15,28,29). Here, we have adapted this approach to enable detection of promoter unwinding in solution at the single-molecule level in real-time, and we designate our adaptation of the approach "single-molecule unwinding-induced fluorescence enhancement" (smUIFE), to underscore the similarity to the established method of single-molecule protein-induced fluorescence enhancement (smPIFE; 30; Figure 1A).

First, we analyzed a promoter DNA fragment having Cy3 incorporated at a site at the downstream edge of the transcription bubble (non-template strand position +2) of a consensus σ^{70} -dependent bacterial promoter (lacCONS-[+2 Cy3]; Figure 1-figure Supplement 1A). Upon adding the Cy3-containing promoter DNA fragment to *E. coli* RNAP- σ^{70} holoenzyme immobilised on a coverslip mounted in a total-internal-reflection fluorescence (TIRF) microscope, we detected the appearance of

fluorescence signal from single fluorescent species, indicating binding of single molecules of Cy3-containing promoter DNA fragment to surface-immobilised single molecules of RNAP holoenzyme (Figure 1A, bottom). Control experiments show that: (i) Cy3-containing promoter DNA fragments bound exclusively to immobilised RNAP molecules (Figure 1-figure Supplement 2A), and the majority (~60%) of the resulting complexes were resistant to challenge with heparin (Figure 1-figure Supplement 2B); (ii) binding of Cy3-containing non-promoter DNA fragments to immobilised RNAP holoenzyme molecules did not result in heparin-resistant complexes (Figure 1-figure Supplement 2C); and (ii) binding of Cy3-containing promoter DNA fragments to immobilised RNAP core enzyme molecules did not result in heparin-resistant complexes (Figure 1-figure Supplement 2D). These results confirm that sequence-specific, heparin-resistant, complexes were formed only between RNAP holoenzyme and Cy3-containing promoter DNA fragments.

We extracted intensity-vs-time-trajectories for the formation of RNAP-promoter complexes, and identified different classes of trajectories. A large class of trajectories (~45%) was characterised by the appearance of a fluorescence intensity of ~200 counts, followed by an increase in fluorescence intensity to ~450 counts, followed by either a decrease of the intensity to ~200 counts or a disappearance of the intensity (Figure 1B, top left; Figure 1-figure Supplement 3, *middle*). Control experiments show that (i) binding of Cy3-containing non-promoter DNA fragments to immobilised RNAP holoenzyme did not result in ≥ 2 -fold fluorescence enhancement (Figure 1-figure Supplement 3C); and (ii) binding of Cy3-containing promoter DNA fragments to immobilised RNAP core molecules did not result in ≥ 2 -fold fluorescence enhancement events for the overwhelming majority of the time-trajectories (~96%; Figure 1-figure Supplement 3D). These results indicate that the detected ~2-fold fluorescence enhancement events represent sequence-specific complexes between RNAP holoenzyme and promoter DNA fragments. Therefore, we assigned the states with no intensity as species that lack promoter DNA or that have promoter DNA with photobleached Cy3; the states with an intensity level of ~200 counts as RNAP-promoter complexes having double-stranded DNA at the Cy3 incorporation site; and states with an intensity level ~450 counts as RNAP-promoter complexes having single-stranded DNA at the Cy3 incorporation site. This assignment yields a

reaction sequence comprising: binding of double-stranded promoter DNA to RNAP (~200 counts; "pre-unwinding state"), followed by promoter unwinding (~450 counts; "unwound state"), followed by promoter rewinding (~200 counts) or probe photobleaching (~0 counts). Upon addition of an NTP subset enabling synthesis of transcripts up to 11-nt in length (ATP, UTP and GTP), ~49% of trajectories showed formation of a stable unwound-promoter state (with fluorescence intensity similar to that of the sub-population exhibiting promoter unwinding), as expected for the formation of initial transcribing complexes ($RP_{itc} \leq 11$; Figure 1-figure Supplement 3B, top; see also Methods). Upon subsequent addition of a separate NTP subset (GTP and CTP), enabling synthesis of transcripts up to 14-nt in length, ~27% of the resulting complexes showed formation of a stable rewound-promoter state (Figure 1-figure Supplement 3B, bottom), as expected for promoter escape and formation of a transcription elongation complex. The results show that RNAP-promoter complexes formed in these experiments are transcriptionally active and are competent for promoter escape (see also Methods).

Focussing on the class of trajectories that showed promoter unwinding after binding (as opposed to other classes of trajectories that did not show promoter unwinding after binding; Figure 1-figure Supplement 3 and *Methods*), we analysed trajectories further to define the kinetics of promoter unwinding (see *Methods*). Using Hidden Markov Modelling (HMM; 31), we extracted dwell times for the pre-unwinding states and plotted a dwell-time histogram (Figure 1B, *top right*). The dwell-time histogram showed a peaked distribution, indicating a non-Markovian process having more than one rate-limiting steps before the formation of the unwound state (32). We fitted this histogram to a two-exponential function (see Methods for a detailed explanation; 32), and estimated the total time spent in the pre-unwinding state to be ~7.5 s (Figure 1B, *top right*; Figure 1D).

To assess whether the assay reports accurately on the kinetics of promoter unwinding, we analyzed altered promoter derivatives predicted to unwind *more quickly* or *more slowly* than lacCONS. To accelerate unwinding, we lowered the energy barrier for unwinding by introducing a non-complementary sequence at positions -10 to -4 relative to the transcription start site (pre-unwound lacCONS-[+2 Cy3]; Figure 1-figure Supplement 1). Time-trajectories for pre-unwound lacCONS-[+2 Cy3] were qualitatively similar to those for lacCONS-[+2 Cy3] in terms of the intensity increase

(Figures 1B, *middle left*, S4A) and the shape of the dwell-time histogram (Figure 1B, *middle right*); however, the trajectories showed significantly shorter dwell times in the pre-unwinding state (~2.8 s vs. ~7.5 s; Figure 1B, *middle right* vs. *top right*). To decelerate the process, we raised the energy barrier for unwinding by introducing a G/C-rich sequence at positions -4 to +1 relative to the transcription start site (G/C lacCONS-[+2 Cy3]; Figure 1-figure Supplement 1). Time-trajectories for G/C lacCONS-[+2 Cy3] showed significantly longer dwell times in the pre-unwinding state (~18.8 s vs. 7.5 s; Figure 1B, *bottom right* vs. *top right*; Figure 1D). Taken together, these results show that dwell times in the pre-unwinding state depend on energy barriers for promoter unwinding, consistent with expectation that the dwell times report on the kinetics of promoter unwinding.

Next, to determine whether promoter unwinding occurs in one step, or in more than one step, we assessed whether unwinding of the upstream half of the transcription bubble (positions -11 to -5) coincides with, or does not coincide with, unwinding of the downstream half of the transcription bubble (positions -4 to +2). To probe unwinding of the upstream half of GC promoter bubble, we performed analogous smUIFE experiments using promoter derivatives having Cy3 incorporated in the upstream half of the transcription bubble, at template-strand position -9 (lacCONS-[-9 Cy3] and G/C lacCONS-[-9 Cy3]; and Figure 1-figure Supplement 1). The resulting trajectories were similar in terms of intensity increases (Figure 1-figure Supplement 4B) and dwell-time-distribution shapes to those obtained with promoter DNA fragments having Cy3 incorporated in the downstream edge of the transcription bubble, but the dwell times in the pre-unwinding state were significantly shorter: ~5.5 s vs. ~7.5 s for lacCONS-[-9 Cy3] vs. lacCONS-[+2 Cy3] (Figure 1C, *top right* vs. Figure 1B, *top right*; Figure 1D) and ~6.0 s vs. ~18.8 s for G/C lacCONS-[-9 Cy3] vs. G/C lacCONS-[+2 Cy3] (Figure 1C, *bottom right* vs. Figure 1B, *bottom right*; 1D). We conclude that, for the promoters analyzed, unwinding of the upstream half of the transcription bubble occurs faster than unwinding of the downstream half of the transcription bubble, and we conclude that we can estimate from our data both the reaction time required for unwinding of the upstream half of the transcription bubble, $t_{\text{UNWIND-UP}}$, (from the lifetime of the pre-unwinding state when Cy3 is incorporated at position -9; ~5.5 s for lacCONS), and the reaction time required for the subsequent unwinding of the downstream half of the

transcription bubble, $t_{\text{UNWIND-DOWN}}$, (from the difference in lifetimes between the pre-unwinding state when Cy3 is incorporated at position +2 and the pre-unwinding state when Cy3 is incorporated at position -9; ~2.0 s for lacCONS; Figure 1D). Our results confirm previous results (16,17,27, 33-36), indicating that promoter unwinding proceeds in a step-wise fashion, in an upstream-downstream direction, and suggest that the step for upstream unwinding is slower than downstream unwinding for lacCONS (~5.5 s vs. ~2.0 s), whereas the step for downstream unwinding is slower than upstream unwinding for G/C lacCONS (~6.0 s vs. ~13.0 s).

Single-molecule unwinding-induced fluorescence enhancement (smUIFE) in the presence of an inhibitor that prevents RNAP clamp opening

To determine whether promoter unwinding is affected by preventing opening of the RNAP clamp, we repeated our experiments in presence of myxopyronin (Myx; 14, 15, 24, 37-38), an RNAP inhibitor that prevents RNAP clamp opening (14, 24, 37; state with an smFRET efficiency, $E^* \sim 0.36$ in Figure 2-figure Supplement 1D) and that allows formation of heparin-sensitive RNAP-promoter complexes but prevents formation of heparin-resistant RNAP-promoter complexes (37; Figures S5A-B). We reasoned that, if clamp opening is obligatory for promoter unwinding, preventing clamp opening by addition of Myx should either prevent or delay downstream unwinding. We first performed smUIFE experiments in the presence of Myx using promoter DNA fragment lacCONS-[+2 Cy3], which has Cy3 incorporated at the downstream edge of the transcription bubble. The results showed a fluorescence intensity enhancement of ~2.4-fold, consistent with unwinding of the downstream edge of the transcription bubble (Figure 2B, *bottom*; Figure 2-figure Supplement 1C; see 15) and showed a dwell time between initial binding and intensity enhancement of ~4.1 s (Figure 2C, *bottom*). We next performed smUIFE experiments in the presence of Myx using promoter DNA fragment lacCONS-[-9 Cy3], which has Cy3 incorporated in the upstream half of the transcription bubble. The results were essentially identical: a fluorescence intensity enhancement of ~2.4 fold (Figure 2B, *top*; Figure 2-figure Supplement 1C, *top*) and a dwell time between initial binding and intensity enhancement of ~4.0 s (Figure 2C). For both promoter derivatives, the observed fluorescence intensity enhancements were similar in the absence and presence of Myx (Figures S4A-B, *top panels* vs. Figure 2-figure

Supplement 1C), and the observed dwell times between initial binding and intensity enhancement times were shorter--not longer--in the presence of Myx than in the absence of Myx (~3.5 s shorter for transcription-bubble downstream edge and ~1.5 s shorter for transcription-bubble upstream half; Figures 2B-C vs. Figures 1B-C, *top panels*). We suggest that Myx prevents formation of heparin-resistant open complexes either by preventing loading of unwound DNA into active centre cleft or by preventing subsequent locking of the RNAP clamp. We infer--contrary to the models in which clamp opening is obligatory for promoter unwinding--that preventing RNAP clamp opening does not prevent promoter unwinding, and increases, not decreases, the kinetics of promoter unwinding.

Single-molecule fluorescence resonance energy transfer (smFRET)

To assess *directly* whether RNAP clamp motions occur during RPo formation, we performed single-molecule fluorescence resonance energy transfer (smFRET) measurements using an RNAP derivative containing Cy3B, serving as a fluorescence donor, incorporated at the tip of the RNAP clamp and Alexa647, serving as a fluorescence acceptor, incorporated at the tip of the opposite wall of the RNAP active-center cleft, monitoring smFRET efficiency (E^*) during RPo formation (Figure 3A). In previous smFRET studies using the same probes, we showed that the RNAP clamp interconverts between open ($E^* \sim 0.2$), partly-closed ($E^* \sim 0.3$), and closed ($E^* \sim 0.4$) conformations in solution (14, 23-25). To monitor RNAP clamp motions during the formation of RPo, we immobilised promoter DNA molecules (biotin-lacCONS; Figure 1-figure Supplement 1, Figure 3-figure Supplement 1) on a coverslip mounted on a TIRF microscope, started recording, and added the doubly-labelled RNAP (Figure 3A). Binding of doubly-labelled RNAP molecules to DNA was monitored by detecting the simultaneous appearance of donor and acceptor fluorescence emission signals on the surface, and RNAP clamp motions in RNAP-promoter complexes at and after binding were monitored by quantifying E^* (Figure 3-figure Supplement 2A). Control experiments show that: (i) doubly-labelled RNAP molecules bound exclusively to immobilised promoter DNA molecules (Figure 3-figure Supplement 1A); (ii) the majority (~87%) of the resulting complexes were resistant to challenge with heparin (Figure 3-figure Supplement 1B); and (iii) doubly-labelled RNAP molecules did not bind stably to immobilised non-promoter DNA molecules (Figure 3-figure Supplement 2C). These results

indicate sequence-specific, heparin-resistant RNAP-promoter complexes were only formed between the doubly labelled RNAP holoenzyme molecules and promoter DNA fragments.

In order to determine the RNAP clamp conformations immediately upon initial binding of RNAP to promoter DNA, we plotted distributions of E^* values for the first five frames (0.5 s) after initial binding. The resulting distributions could be fitted to a Gaussian function with mean E^* of ~ 0.4 , indicating that the initial binding of RNAP to promoter DNA involved RNAP with a closed clamp (Figure 3-figure Supplement 2B). Next, we examined full E^* time-trajectories, for up to ~ 60 s, following initial binding, seeking E^* changes potentially consistent with RNAP clamp opening. We detected no E^* changes--not even transient E^* changes, within the ~ 100 ms temporal resolution of the analysis--that potentially could be assigned as consistent with clamp opening (E^* of ~ 0.2 ; Figure 3B, area highlighted in cyan; Figure 3-figure Supplement 2A).

Next, we examined full E^* time-trajectories, following initial binding, seeking any E^* changes potentially consistent with any RNAP clamp motions (see *Methods* and Figure 3-figure Supplement 3 for full classification). Intriguingly, a large fraction of trajectories ($\sim 44\%$) started at $E^* \sim 0.40$, indicative of the previously defined closed clamp state, then transitioned to $E^* \sim 0.48$, indicative of a new, more tightly closed, clamp state, and then returned to $E^* \sim 0.40$ or photobleached (Figures 3B-C; Figure 3-figure Supplement 3B, *top*). We refer to the new, more tightly closed, clamp state with $E^* \sim 0.48$, as the “locked-clamp” state. We further analysed E^* time-trajectories to determine the time between initial binding of RNAP to promoter DNA and appearance of the locked-clamp state. The corresponding dwell-time histogram showed a peaked distribution and was fitted to a two-exponential function, yielding ~ 7.8 s, as the time between initial binding of RNAP to promoter DNA and appearance of the locked-clamp state (Figure 3D), a time that, within error, is identical to the ~ 7.5 s time between initial binding and unwinding of the downstream half of the transcription bubble.

Analogous experiments with a promoter derivative having G/C-rich sequence at positions -4 to $+1$ relative to the transcription start site, G/C lacCONS, yielded similar results: i.e., initial binding by RNAP with a closed-clamp state ($E^* \sim 0.41$; Figure 3-figure Supplement 4A; B, *left*); no trajectories

showing transitions --not even transient transitions, within the ~400 ms temporal resolution of the analysis--to an open-clamp state during a period up to ~200 s after initial binding; a large fraction of trajectories (~48%), showing a transition to a locked-clamped state ($E^* \sim 0.50$, Figure 3-figure Supplement 4A; B, *right*), and a time between initial binding and appearance of the locked-clamped state matching the time required for unwinding of the downstream half of the transcription bubble (Figures 3E, Figure 3-figure Supplement 4C).

We conclude that the RNAP clamp is in a closed state upon promoter binding, that the RNAP clamp does not open--not even transiently, within the temporal resolution of our analysis--between promoter binding and promoter unwinding, and that the RNAP clamp closes further--"locks"--after promoter unwinding.

Discussion

Taken together, our results indicate that RPo formation by *E. coli* RNAP- σ^{70} holoenzyme at a consensus bacterial core promoter proceeds through a “*bind-unwind-load-and-lock*” mechanism, in which the RNAP clamp is closed upon promoter binding, remains closed during unwinding of promoter DNA--which proceeds in an upstream-to-downstream direction--and then closes further, locking the unwound DNA in the RNAP active-centre cleft (Figure 4).

As described in the introduction, it has been the predominant view that structural considerations necessitate RNAP clamp opening for loading of dsDNA into the RNAP active-centre cleft but do not necessitate RNAP clamp opening for loading of ssDNA into the RNAP active-centre cleft (1-2,7-9,11,13-14). Under that predominant view, our finding that the RNAP clamp remains closed throughout promoter unwinding at a consensus bacterial promoter implies that it is ssDNA, not dsDNA, that enters the RNAP active-centre-cleft, and thus that promoter unwinding occurs at least in part outside, not inside, the RNAP active-centre cleft (Figure 4).

In contrast to the predominant view, it recently has been speculated, based on molecular-dynamics simulations, that part of the RNAP cleft potentially could become accessible to both dsDNA and ssDNA without clamp opening, due to motions, putatively occurring on the nanosecond time-scale, of

the RNAP β lobe ("gate opening"; 39). Under this alternative view, our finding that the RNAP clamp remains closed throughout promoter unwinding at a consensus bacterial promoter potentially could be consistent with either ssDNA or dsDNA entering the RNAP active-centre-cleft, and thus potentially could be consistent with promoter unwinding that occurs either outside or inside, the RNAP active-centre cleft. Nevertheless, in view of the absence of experimental support for the alternative view, and in view of the mismatch between the nanosecond time scale of the limiting reaction in the alternative view and the millisecond-to-second time scales of promoter unwinding, we tend to disfavour this alternative view.

The consensus bacterial promoter employed in this study has been used in previous work to define transcription mechanisms, including RNAP clamp closure upon RPo formation (14), DNA scrunching in transcription-start-site selection (40), DNA scrunching in initial transcription (41), and RNAP pausing in initial transcription (42,43), all of which subsequently were validated for other promoters. Nevertheless, we emphasize that it remains to be determined whether the bind-unwind-load-and-lock pathway defined here for the consensus bacterial promoter also is used by *E. coli* RNAP σ^{70} holoenzyme at other promoters and by other *E. coli* RNAP holoenzymes. Consistent with the possibility that a similar mechanism is used by *E. coli* RNAP σ^{70} holoenzyme at other promoters, a recent cryo-EM study of transcription initiation by *E. coli* RNAP σ^{70} holoenzyme at another promoter, *rpsT* P2, identified structural states having a partly unwound transcription bubble and a closed RNAP clamp (17). We note that the smUIFE and smFRET methods reported in this work could be applied to analyze transcription initiation by any *E. coli* RNAP holoenzyme at any promoter and potentially could be adapted to analyze transcription initiation by any RNAP--bacterial, archaeal, or eukaryotic--at any promoter. Extension of these assays using more complex labelling and imaging schemes should allow simultaneous observation of promoter unwinding and RNAP clamp conformational changes in the same molecule, enabling a more detailed view of the coupling of the molecular motions involved in promoter unwinding. Finally, development of massively parallel single-molecule assays interrogating large libraries of promoter sequences, would enable a comprehensive analysis of

general and specific features of this first step in transcription initiation for different promoter sequences.

Methods

Preparation of reagents: RNAP, Oligodeoxyribonucleotides, Myxopyronin

RNAP derivatives: For experiments in Figures 1, 2, S2-S5, hexahistidine-tagged *Escherichia coli* RNAP holoenzyme was prepared using co-expression of genes encoding RNAP β' , β , α , ω and σ^{70} subunits to afford an RNAP σ^{70} holoenzyme derivative as follows: single colonies of *E. coli* strain BL21(DE3) (Millipore) co-transformed with plasmid pV10 (44) and plasmid pRSFduet-sigma (45) were used to inoculate 20 ml LB broth (46) containing 100 μ g/ml ampicillin and 50 μ g/ml kanamycin and cultures were incubated 16 h at 37°C with shaking. Culture aliquots (2x10 ml) were used to inoculate LB broth (2x1 L) containing 100 μ g/ml ampicillin and 50 μ g/ml kanamycin; cultures were incubated at 37°C with shaking until OD₆₀₀ = 0.6; IPTG was added to 1 mM; and cultures were further incubated 3.5 h at 37°C with shaking. Cells were harvested by centrifugation (4,000 x g; 20 min at 4°C), re-suspended in 20 ml buffer A (10 mM Tris-HCl, pH 7.9, 200 mM NaCl, and 5% glycerol), and lysed using an EmulsiFlex-C5 cell disrupter (Avestin). The lysate was cleared by centrifugation (20,000 x g; 30 min at 4°C), precipitated with polyethyleneimine (Sigma-Aldrich) as in (47), and precipitated with ammonium sulfate as in (47). The precipitate was dissolved in 30 ml buffer A and loaded onto a 5-ml column of Ni-NTA-agarose (Qiagen) pre-equilibrated in buffer A; the column was washed with 50 ml buffer A containing 10 mM imidazole, and eluted with 25 ml buffer A containing 200 mM imidazole. The sample was further purified by anion-exchange chromatography on Mono Q 10/100 GL (GE Healthcare; 160 ml linear gradient of 300-500 mM NaCl in 10 mM Tris-HCl, pH 7.9, 0.1 mM EDTA, and 5% glycerol; flow rate = 2 ml/min). Fractions containing hexahistidine-tagged *E. coli* RNAP σ^{70} holoenzyme were pooled, concentrated to ~2 mg/ml using 30 kDa MWCO Amicon Ultra-15 centrifugal ultrafilters (EMD Millipore), and stored in aliquots at -80°C.

For experiments in Figures 3 and Figure 3-figure Supplements 1-4, fluorescently labelled, hexahistidine-tagged *E. coli* RNAP holoenzyme (hereafter 'labeled-RNAP') with Cy3B and Alexa647 at positions 284 on the β' subunit, and 106 on the β subunit, respectively, was prepared using in-vivo reconstitution methods as described (23).

Nucleic acids: Oligodeoxyribonucleotides were purchased from IBA Lifesciences, dissolved in nuclease-free water (Ambion) to a final concentration of 100 μ M and stored at -20°C.

Oligodeoxyribonucleotides used in Figures 1, Figure 1-figure Supplements 2-4, and Figure 2-figure Supplement 1, were labelled with Cy3 N-hydroxysuccinimidyl (NHS) ester (Fisher Scientific) as described (48). Oligodeoxyribonucleotides were annealed by mixing two complementary strands in a ratio of 1:1 in hybridization buffer (50 mM Tris-HCl pH 8.0, 500 mM NaCl, 1 mM EDTA) and by heating for 5 min at 95°C, followed by cooling to 25°C in 2°C steps with 1 min per step using a thermal cycler (Applied Biosystems).

Myxopyronin was prepared as described (37).

Single-molecule fluorescence microscopy: smUIFE experiments

For experiments in Figures 1, 2, Figure 1-figure Supplements 2-4, and Figure 2-figure Supplement 1, observation wells for real-time experiments were prepared as described (23). Briefly, a biotin-PEG-passivated glass surface was prepared, functionalized with Neutravidin (Sigma Aldrich), and treated with biotinylated anti-hexahistidine monoclonal antibody (Penta-His Biotin Conjugate; Qiagen), yielding wells with (biotinylated anti-hexahistidine monoclonal antibody)-Neutravidin-biotin-PEG-functionalised glass floors. Hexahistidine tagged RNAP σ^{70} holoenzyme molecules were immobilised in observation wells with (biotinylated anti-hexahistidine monoclonal antibody)-Neutravidin-biotin-PEG-functionalized glass floors, as follows: aliquots (30 μ l) of 0.1 nM hexahistidine tagged RNAP σ^{70} holoenzyme in KG7 buffer (40 mM HEPES-NaOH, pH 7.0, 100 mM potassium glutamate, 10 mM MgCl₂, 1 mM dithiothreitol, 100 μ g/ml bovine serum albumin, and 5% glycerol) were added to the observation chamber and incubated 2-4 min at 22°C, solutions were removed, wells were washed

407 with 2 x 30 μ l KG7, and 30 μ l KG7 imaging buffer (KG7 buffer containing 2 mM Trolox, 1 mg/ml
 408 glucose oxidase, 40 μ g/ml catalase, and 1.4% w/v D-glucose) at 22°C was added.

409 For experiments in Figure 1-figure Supplement 2, Cy3-labelled promoter (or non-promoter)
 410 fragments were manually added (final concentration of 2 nM) to the observation wells containing
 411 immobilised RNAP σ^{70} holoenzyme (or RNAP core enzyme) molecules and incubated for 5 min;
 412 wells were then washed with KG7 and movies were recorded. Next, observation wells containing
 413 RNAP-promoter complexes were supplemented with KG7 containing 250 μ g/ml heparin (Sigma
 414 Aldrich) solution, incubated for 1 min; wells were then washed with KG7 and movies were recorded.

415 For experiments monitoring RNAP-promoter complex formation reactions in real time (Figures 1, 2,
 416 Figure 1-figure Supplement 3 and Figure 2-figure Supplement 1), observation wells containing
 417 immobilised RNAP were supplemented with KG7 imaging buffer, recordings were started, and Cy3-
 418 labelled promoter (or non-promoter) fragments were manually added (using a pipette) to the
 419 observation wells during the recording so as to yield a final concentration of 2 nM of Cy3-labelled
 420 DNA in the wells. For experiments in Figure 2-figure Supplement 1 A-C, same procedures were
 421 followed, except that KG7 imaging buffer was supplemented with 20 μ M Myxopyronin.

422 For experiments in Figure 1-figure Supplement 3B top panel, observation wells containing
 423 immobilised RNAP-promoter complexes (formed with LC-[+2-Cy3]; sequence in Figure 1-figure
 424 Supplement 1) were supplemented with KG7 buffer containing a NTP subset (500 μ M ApA and
 425 100 μ M each of ATP, GTP and UTP) directing synthesis of RNA up to position +11(RPitc \leq 11),
 426 incubated for 5 min at 22°C, solutions were removed, wells were washed with 2 x 30 μ l KG7, and
 427 30 μ l KG7 imaging buffer at 22°C was added. Movies of complexes corresponding to stalled
 428 RPitc \leq 11 molecules were recorded. For experiments in Figure 1-figure Supplement 3B bottom
 429 panel, observation wells containing immobilised stalled RPitc \leq 11 molecules were supplemented
 430 with KG7 imaging buffer, the recording of a movie was started, and an NTP subset (100 μ M each
 431 of GTP and CTP) directing extension of stalled complexes with 11-mer RNA to a 14-mer RNA,
 432 was added in real time. Extension of RNA up to +11 results in stalled initial transcribing

complexes (49) and extension of RNA to +14 results in promoter escape and leads to formation of stalled elongation complexes for the lacCONS promoter used (Wang, Mazumder et al., in preparation).

Single-molecule fluorescence microscopy: smFRET experiments

For experiments in Figure 3 and Figure 3-figure Supplements 1-4, observation wells of biotin-PEG passivated glass surface was prepared and functionalized with Neutravidin (Sigma Aldrich) to yield Neutravidin-biotin-PEG-functionalised glass floors. Biotin-tagged promoter DNA fragments were then immobilised in these observation wells as follows: aliquots (30 μ l) of 0.05 nM biotin-tagged promoter fragments in KG7 were added to the observation chamber and incubated 1 min at 22°C, solutions were removed, wells were washed with 2 x 30 μ l KG7, and 30 μ l KG7 imaging buffer at 22°C was added.

For experiments in Figure 3-figure Supplement 16, clamp-labelled RNAP molecules were manually added (final concentration of 2 nM) to the observation wells containing immobilised promoter DNA fragments, incubated for 5 min, wells were washed with KG7 and movies were recorded. Next, observation wells containing RNAP-promoter complexes were supplemented with KG7 containing 250 μ g/ml heparin solution, incubated for 1 min, wells were washed with KG7 and movies were recorded.

For experiments monitoring RNAP-promoter complex formation reactions in real time (Figures 3 and Figure 3-figure Supplements 2-4, observation wells containing immobilised promoter (or non-promoter) fragments were supplemented with KG7 imaging buffer, recordings were started, and labeled-RNAP molecules (with Cy3B and Alexa647 at positions 284 on the β' subunit, and 106 on the β subunit of RNAP σ^{70} holoenzyme) were manually added (using a pipette) to the observation wells during the recording so as to yield a final concentration of 2 nM of labeled RNAP in the wells.

Single-molecule fluorescence microscopy: data collection

Single-molecule fluorescence experiments were performed using a custom-built objective-type total-internal-reflection fluorescence (TIRF) microscope (50). Light from a green laser (532 nm;

Samba; Cobolt) and a red laser (635 nm; CUBE 635-30E, Coherent) was combined using a dichroic mirror coupled into a fiber-optic cable focused onto the rear focal plane of a 100x oil-immersion objective (numerical aperture 1.4; Olympus) and was displaced off the optical axis, such that the incident angle at the oil-glass interface of a stage-mounted observation chamber exceeded the critical angle, thereby creating an exponentially decaying evanescent wave (51). Alternating-laser excitation (ALEX; 52,53) was implemented by directly modulating the green and red lasers using an acousto-optical modulator (1205C, Isomet). Fluorescence emission was collected from the objective, was separated from excitation light using a dichroic mirror (545 nm/650 nm, Semrock) and emission filters (545 nm LP, Chroma; and 633/25 nm notch filter, Semrock), was focused on a slit to crop the image, and then was spectrally separated (using a dichroic mirror; 630 nm DLRP, Omega) into donor and emission channels focused side-by-side onto an electron-multiplying charge-coupled device camera (EMCCD; iXon 897; Andor Technology). A motorized x/y-scanning stage (MS-2000; ASI) was used to control the sample position relative to the objective.

For experiments in Figures 1-2, Figure 1-figure Supplements 2-4 and Figure 2-figure Supplement 1, frame rates were either 50-ms or 200-ms, and laser powers were either 0.60 mW or 0.15 mW at 532 nm. For experiments in Figure 3 and Figure 3-figure Supplement 2-3, frames were either 100-ms or 200-ms long, and laser powers were either 200 μ W in red, 500 μ W in green, or 80 μ W in red, 200 μ W in green, respectively. For experiments in Figure 3-figure Supplement 4, frame rates were 400-ms long, and laser powers were 50 μ W in red, 150 μ W in green. All data acquisition was carried out at 22°C.

Single-molecule fluorescence microscopy: data analysis for smUIFE experiments

For experiments in Figures 1-2, Figure 1-figure Supplements 2-4 and Figure 2-figure Supplement 1, localisation of single fluorescence emitters was detected and background-corrected fluorescence intensity-vs-time trajectories from each localisation were extracted and curated to exclude trajectories exhibiting very high fluorescence intensities (I_{Cy3}) upon binding ($I_{Cy3} > 750$ photon counts), trajectories exhibiting multiple binding events during the observation window and trajectories exhibiting photoblinking. Initial inspection of time-trajectories for experiments with lacCONS-[+2 Cy3],

revealed three main classes of molecules. Class-I molecules started with the appearance of signal having intensity of ~200 photon counts, which remained stable until its disappearance (~46%; Figure 1-figure Supplement 3, *top*). Class-II molecules also started with appearance of a signal having intensity of ~200 photon counts, followed by intensity increase to ~450 photon counts after some time, followed by either signal disappearance or intensity decrease to ~200 photon counts (~45%; Figures 1B, Figure 1-figure Supplement 3, *middle*). Class-III molecules started with appearance of a signal having intensity of ~450 photon counts, followed by intensity decrease to ~220 photon counts, and subsequent signal disappearance, or intensity increase to ~450 photon counts (~9%; Figure 1-figure Supplement 3, *bottom*). Similar observations were made for all other Cy3-labelled promoters studied.

Based on intensity levels, we assigned states with no signal to absence of a promoter DNA or to a bleached probe; states with ~200 photon counts to a promoter DNA that is double stranded (dsDNA) in the Cy3 vicinity; and states with ~450 counts to a promoter that is unwound in the Cy3 vicinity. We thus assigned events in Class-I molecules to binding of a promoter DNA molecule to RNAP, followed by dissociation of complexes, indicating formation of non-specific complexes; these events are also consistent with bleaching occurring prior to any intensity increase. We assigned events in Class-II molecules to binding of a promoter DNA molecule to RNAP, followed by promoter unwinding, followed by bleaching or promoter rewinding. Finally, we assigned events in Class-III molecules to binding of an unwound promoter DNA molecule to RNAP, followed by promoter rewinding, followed by bleaching or promoter unwinding, indicating formation of complexes where the initial unwinding event is missed. We further curated intensity time-trajectories up to the point of initial ~2-fold intensity enhancement for Class-II molecules only, since they showed an unambiguous bubble-opening event after initial binding.

Next, photon counts (I_{Cy3}) for the set of curated intensity-vs-time trajectories were divided by 1000 to obtain I_{Cy3}^* ; the corresponding I_{Cy3}^* -vs-time trajectories were analyzed to identify the different fluorescence intensity states using Hidden Markov Modelling (HMM) as implemented in the MATLAB (MathWorks) software package ebFRET (54) using a three-state model (one of which

corresponds to a negligible I_{Cy3}^* state). The intensity I_{Cy3}^* , for each of the other two HMM-derived states were extracted from ebFRET and converted to I_{Cy3} values, which in turn were binned and plotted as I_{Cy3} count histograms (Figure 1-figure Supplement 4, Figure 2-figure Supplement 1C). These histograms were fitted using Gaussian distributions in Origin to define the mean fluorescence intensity that corresponds to each state (Figure 1-figure Supplement 4, Figure 2-figure Supplement 1).

Dwell times for each fluorescence intensity states were extracted from HMM fits to I_{Cy3}^* -vs-time trajectories, were binned, and were plotted as distribution histograms in Origin. For experiments in Figures 1-2, dwell-time distributions corresponding to the pre-unwinding state resembled peaked distributions indicating presence of at least two sub-steps and were fit to a two-exponential function of the form $y = A*(e^{-x/t_1} - e^{-x/t_2})$, where y represents counts of dwells in the closed-bubble state following the initial binding event and before the signal increase event, x represents time, and t_1 and t_2 represent the lifetime of the individual sub-steps. From the fit, we estimate the lifetimes corresponding to the two sub-steps, as well as the total time spent in the first closed-bubble state (as the sum of time spent in the two sub-steps; Figure 2B, right panels).

We note that it is possible that the transition involves more than two steps, but our current analysis and available data sets cannot specify the number and duration of each sub-step; consequently, we interpret qualitatively the shape of the dwell-time histogram as an indication of a multi-step process, and focus on the total time spent before the intensity enhancement event, since that can be interpreted with certainty as: the time taken before unwinding in the vicinity of Cy3.

Single-molecule fluorescence microscopy: data analysis for smFRET experiments

For experiments in Figure 3 and Figure 3-figure Supplements 1-4, localizations in donor-emission (green) and acceptor-emission (red) channels were detected using the peak-finding algorithm of the MATLAB (MathWorks) software package Twotone, as described (50). Peaks detected in both emission channels (i.e., peaks for molecules containing both donor and acceptor probes) were fitted with two-dimensional Gaussian functions to extract background-corrected intensity-vs.-time trajectories for donor-emission intensity upon donor excitation (I_{DD}), acceptor-emission intensity upon

donor excitation (I_{DA}), and acceptor-emission intensity upon acceptor excitation (I_{AA}), as described (50). Intensity-vs.-time trajectories were curated to exclude trajectories exhibiting $I_{DD} < 100$ or $> 1,000$ counts or $I_{AA} < 200$ or $> 1,000$ counts, trajectories exhibiting multiple-step donor or acceptor photobleaching, trajectories exhibiting donor or acceptor photo-blinking and portions of trajectories following donor or acceptor photobleaching. Intensity-vs.-time trajectories were used to calculate trajectories of apparent donor-acceptor smFRET efficiency (E^*) as described (50,52-53):

$$E^* = I_{DA} / (I_{DD} + I_{DA})$$

E^* time trajectories were analyzed globally to identify E^* states by use of HMM as implemented in MATLAB (MathWorks) software package ebFRET (54).

HMM analysis of E^* time-trajectories revealed four types of molecules. The most abundant were Class-I molecules (~45% of all events), that started with $E^* \sim 0.40$, remained at $E^* \sim 0.40$, and then bleached (Figure 3-figure Supplement 3A), and Class-II molecules (~44%) that started with $E^* \sim 0.40$, transitioned to $E^* \sim 0.48$, and then bleached or returned to $E^* \sim 0.40$ (Figure 3-figure Supplement 3B, *top*). More rarely, we observed Class-III molecules (~9% of all events), that started with $E^* \sim 0.48$, transitioned to $E^* \sim 0.40$, followed by bleaching or transition to $E^* \sim 0.48$; Figure 3-figure Supplement 3C), and, very rarely, we observed Class-IV molecules (~2%), which started at $E^* \sim 0.40$, switched between $E^* \sim 0.40$ -0.20 and bleached (Figure 3-figure Supplement 3D).

We refer to the new $E^* \sim 0.48$ state observed here as the “locked-clamp” conformation, with Class-II molecules providing information on the time taken to form the “locked-clamp” conformation; in contrast, Class-I molecules represent RNAP molecules that either bleach before the transition to the locked-clamp state or bind non-specifically to DNA; and Class-III molecules represent molecules where the initial clamp locking is missed.

E^* time trajectories for Class-II molecules, were fitted to a two-state HMM model, E^* -values from the fitted model were extracted, binned and plotted using Origin (Origin Lab), and were fitted to Gaussian distributions using Origin (Figure 3B, right panels and Figure 3-figure Supplement 3B, left panel; colored curves). The resulting histograms provide population distributions of E^* states and, for

each E* state, define mean E* (Figure 3B, right panels and Figure 3-figure Supplement 4B, right panel; colored bars and inset). Dwell-time distributions corresponding to time spent before the first transition from a closed-clamp state to a locked-clamp state were extracted from HMM fits to E*-vs-time trajectories, and were binned and plotted as distribution histograms in Origin (Figure 3 and Figure 3-figure Supplement 4C). Dwell-time histograms obtained in this manner exhibited the shape of a peaked distribution, indicating presence of at least two sub-steps, were fitted to a two-exponential function of the form $y = A*(e^{-x/t_1} - e^{-x/t_2})$, where y represents counts of dwells in the closed-clamp state following the initial binding event and before the clamp-locking event, x represents time, and t_1 and t_2 represent the lifetimes of the individual sub-steps. From the fit, we estimate the time spent in the two sub-steps, as well as the total time before transition to “locked-clamp” conformation (t_{LOCK}) from the sum of times corresponding to the two sub-steps. Similar to the case for fluorescence enhancement experiments described previously, we note that there may be more than two-steps which contribute significantly to these dwell-times, and we could not infer an accurate model in terms of the number and duration of each sub-step involved from this dataset. Therefore, we avoid assigning the two sub-steps to specific conformations or events and focus on the total time spent before the transition to “locked-clamp” conformation.

Data and software availability.

All information for replication is included in the submission and data corresponding to each figure are provided as source data files. MATLAB software packages TwoTone and ebFRET are available on Github (<https://github.com/annawang692/TwoTone2018> and <http://ebfret.github.io/>).

ACKNOWLEDGEMENTS

We thank Dr. Anssi Malinen for discussions and early work on the development of real-time smFRET assays, and Dr. Horst Steuer for the development of custom software. This work was supported by the Wellcome Trust [110164/Z/15/Z to A.N.K.] and NIH [GM041376 to R.H.E.].

Conflict of interest statement. None declared.

References

1. Mazumder, A. and Kapanidis, A.N. (2019) Recent advances in understanding sigma70-dependent transcription initiation mechanisms. *J Mol Biol*, **431**, 3947-3959.
2. Ruff, E.F., Record, M.T., Jr, & Artsimovitch, I. (2015). Initial events in bacterial transcription initiation. *Biomolecules*, **5**, 1035–1062.
3. Bae, B., Feklistov, A., Lass-Napiorkowska, A., Landick, R., Darst, S.A., (2015) Structure of a bacterial RNA polymerase holoenzyme open promoter complex. *eLife*, **4**, p. e08504.
4. Zuo, Y. and Steitz, T.A. (2015) Crystal structures of the E. coli transcription initiation complexes with a complete bubble. *Mol Cell*, **58**, 534-540.
5. Zhang, Y., Feng, Y., Chatterjee, S., Tuske, S., Ho, M.X., Arnold, E., & Ebright, R.H. (2012). Structural basis of transcription initiation. *Science*, **338**, 1076–1080.
6. Feklistov, A. and Darst, S.A. (2011) Structural basis for promoter-10 element recognition by the bacterial RNA polymerase sigma subunit. *Cell*, **147**, 1257-1269.
7. Mekler, V., Kortkhonjia, E., Mukhopadhyay, J., Knight, J., Revyakin, A., Kapanidis, A.N., Niu, W., Ebright, Y.W., Levy, R., Ebright, R.H. (2002) Structural organization of bacterial RNA polymerase holoenzyme and the RNA polymerase-promoter open complex. *Cell*, **108**, 599-614.
8. Murakami K.S., Masuda S., Darst S.A., (2002) Structural basis of transcription initiation: RNA polymerase holoenzyme at 4 Å resolution. *Science*, **296**, 1280-1284.
9. Murakami K. S., Masuda S., Campbell E.A., Muzzin O., Darst S.A., (2002) Structural basis of transcription initiation: an RNA polymerase holoenzyme-DNA complex. *Science*, **296**, 1285-1290.

10. Vassylyev D.G., Sekine S., Laptenko O., Lee J., Vassylyeva M.N., Borukhov S., Yokoyama S., (2002) Crystal structure of a bacterial RNA polymerase holoenzyme at 2.6 Å resolution. *Nature*, **417**, 712-719.
11. Young B.A., Gruber T.M., Gross C.A., (2002) Views of transcription initiation. *Cell*, **109**, 417-420.
12. Murakami K.S., Darst S.A., (2003) Bacterial RNA polymerases: the whole story. *Curr Opin Struct Biol*, **13**, 31-39.
13. Darst, S., Opalka, N., Chacon, P., Polyakov, A., Richter, C., Zhang, G., and Wriggers, W. (2002) Conformational flexibility of bacterial RNA polymerase. *Proc Natl Acad Sci U S A*, **99**, 4296-4301.
14. Chakraborty, A., Wang, D., Ebright, Y.W., Korlann, Y., Kortkhonja, E., Kim, T., Chowdhury, S., Wigneshweraraj, S., Irschik, H., Jansen, R., Nixon, B.T., Knight, J., Weiss, S., & Ebright, R.H. (2012) Opening and closing of the bacterial RNA polymerase clamp. *Science*, **337**, 591-595.
15. Feklistov, A., Bae, B., Hauver, J., Lass-Napiorkowska, A., Kalesse, M., Glaus, F., Altmann, K. H., Heyduk, T., Landick, R., Darst, S.A. (2017) RNA polymerase motions during promoter unwinding. *Science*, **356**, 863-866.
16. Boyaci, H., Chen, J., Jansen, R., Darst, S.A. and Campbell, E.A. (2019) Structures of an RNA polymerase promoter unwinding intermediate elucidate DNA unwinding. *Nature*, **565**, 382-385.
17. Chen, J., Chiu, C., Gopalkrishnan, S., Chen, A.Y., Olinares, P.D.B., Saecker, R.M., Winkelman, J.T., Maloney, M.F., Chait, B.T., Ross, W., Gourse R.L., Campbell E.A, Darst, S.A. (2020) Stepwise promoter unwinding by bacterial RNA Polymerase. *Mol Cell*, **78**, 275-288 e276.
18. Spassky A., Kirkegaard K., Buc H. (1985) Changes in the DNA structure of the lac UV5 promoter during formation of an open complex with Escherichia coli RNA polymerase. *Biochemistry*, **24**, 2723-2731.
19. Duval-Valentin G., Ehrlich R. (1986) Interaction between E. coli RNA polymerase and the tetR promoter from pSC101: homologies and differences with other E. coli promoter systems from close contact point studies. *Nucleic Acids Res* **14**, 1967-1983.
20. Cowing D.W., Mecsas J., Record Jr. M.T., Gross C.A. (1989) Intermediates in the formation of the open complex by RNA polymerase holoenzyme containing the sigma factor sigma 32 at the groE promoter. *J Mol Biol* **210**, 521-530.
21. Schickor P., Metzger W., Werel W., Lederer H., Heumann H. (1990) Topography of intermediates in transcription initiation of *E. coli*. *EMBO J* **9**, 2215-2220.
22. Davis C.A., Bingman C.A., Landick R., Record, Jr. M.T., Saecker R.M. (2007) Real-time footprinting of DNA in the first kinetically significant intermediate in open complex formation by Escherichia coli RNA polymerase. *Proc Natl Acad Sci U S A* **104**, 7833-7838.
23. Lin, W., Das, K., Degen, D., Mazumder, A., Duchi, D., Wang, D., Ebright, Y.W., Ebright, R.Y., Sineva, E., Gigliotti, M. *et al.* (2018) Structural basis of transcription inhibition by Fidaxomicin (Lipiamycin A3). *Mol Cell*, **70**, 60-71 e15.
24. Duchi, D., Mazumder, A., Malinen, A. M., Ebright, R. H., Kapanidis, A. N. (2018) The RNA polymerase clamp interconverts dynamically among three states and is stabilized in a partly closed state by ppGpp. *Nucleic Acids Res*, **46**, 7284-7295.
25. Mazumder, A., Wang, A., Uhm, H., Ebright, R.H., Kapanidis, A.N. (2021) RNA polymerase clamp conformational dynamics: long-lived states and modulation by crowding, cations, and nonspecific DNA binding. *Nucleic Acids Res*, Advance online article.
26. Glyde, R., Ye, F., Jovanovic, M., Kotta-Loizou, I., Buck, M., Zhang, X. (2018) Structures of bacterial RNA Polymerase complexes reveal the mechanism of DNA loading and transcription initiation. *Mol Cell*, **70**, 1111-1120.

27. Rogozina, A., Zaychikov, E., Buckle, M., Heumann, H., Sclavi, B. (2009) DNA melting by RNA polymerase at the T7A1 promoter precedes the rate-limiting step at 37 °C and results in the accumulation of an off-pathway intermediate. *Nucleic Acids Res*, **37**, 5390-5404.
28. Ko, J. and Heyduk, T. (2014) Kinetics of promoter escape by bacterial RNA polymerase: effects of promoter contacts and transcription bubble collapse. *Biochem J*, **463**, 135-144.
29. Koh, H. R., Roy, R., Sorokina, M., Tang, G. Q., Nandakumar, D., Patel, S. S., & Ha, T. (2018). Correlating Transcription Initiation and Conformational Changes by a Single-Subunit RNA Polymerase with Near Base-Pair Resolution. *Mol cell*, **70**, 695–706.
30. Hwang, H., & Myong, S. (2014). Protein induced fluorescence enhancement (PIFE) for probing protein-nucleic acid interactions. *Chemical Society reviews*, **43**, 1221–1229.
31. Van de Meent, J.W., Bronson J.E., Wiggins C.H., Gonzalez R.L. Jr. (2014) Empirical Bayes methods enable advanced population-level analyses of single-molecule FRET experiments. *Biophys J*, **106**, 1327-1337.
32. Floyd, D. L., Harrison, S.C., van Oijen, A.M. (2010) Analysis of kinetic intermediates in single-particle dwell-time distributions. *Biophys J*, **99**, 360–366.
33. Suh, W.C., Ross, W., Record, M.T. Jr. (1993) Two open complexes and a requirement for Mg²⁺ to open the lambda PR transcription start site. *Science*, **259**, 358-61.
34. Helmann, J.D., deHaseth, P.L. Protein-nucleic acid interactions during open complex formation investigated by systematic alteration of the protein and DNA binding partners. (1999) *Biochemistry*, **1999**, 38, 5959-67.
35. Lim, H. M., Lee, H. J., Roy, S., & Adhya, S. (2001). A "master" in base unpairing during isomerization of a promoter upon RNA polymerase binding. *Proc Natl Acad Sci U S A*, **98**, 14849–14852.
36. Auner H., Buckle M., Deufel A., Kutateladze T., Lazarus L., Mavathur R., Muskhelishvili G., Pemberton I., Schneider R., Travers A. (2003) Mechanism of transcriptional activation by FIS: role of core promoter structure and DNA topology. *J Mol Biol*, **331**, 331–344.
37. Mukhopadhyay J., Das K., Ismail S., Koppstein D., Jang M., Hudson B., Sarafianos S., Tuske S., Patel J., Jansen R., Irschik H., Arnold E., Ebright R.H. (2008) The RNA polymerase "switch region" is a target for inhibitors. *Cell*, **135**, 295-307.
38. Belogurov G.A., Vassilyeva M.N., Sevostyanova A., Appleman J.R., Xiang A.X., Lira R., Webber S.E., Klyuyev S., Nudler E., Artsimovitch I., Vassilyev D.G. (2009) Transcription inactivation through local refolding of the RNA polymerase structure. *Nature*, **457**, 332-335.
39. Unarta, I.C., Cao, S., Kubo, S., Wang, W., Cheung, P.P., Gao, X., Takada, S., Huang, X. (2021) Role of bacterial RNA polymerase gate opening dynamics in DNA loading and antibiotics inhibition elucidated by quasi-Markov State Model. *Proc Natl Acad Sci USA*; Apr 27, 118.
40. Winkelman, J. T., Vvedenskaya, I. O., Zhang, Y., Zhang, Y., Bird, J. G., Taylor, D. M., Gourse, R. L., Ebright, R. H., & Nickels, B. E. (2016) Multiplexed protein-DNA cross-linking: Scrunching in transcription start site selection. *Science*, **351**, 1090–1093.
41. Kapanidis, A. N., Margeat, E., Ho, S. O., Kortkhonja, E., Weiss, S., & Ebright, R. H. (2006). Initial transcription by RNA polymerase proceeds through a DNA-scrunching mechanism. *Science*, **314**, 1144–1147.
42. Duchi D, Bauer D.L., Fernandez L., Evans G., Robb N., Hwang L.C., Gryte K., Tomescu A., Zawadzki P., Morichaud Z., Brodolin K., Kapanidis A.N. (2016) RNA Polymerase Pausing during Initial Transcription. *Molecular cell*, **63**, 939-50.
43. Winkelman, J. T., Pukhrambam, C., Vvedenskaya, I. O., Zhang, Y., Taylor, D. M., Shah, P., Ebright, R. H., & Nickels, B. E. (2020) XACT-Seq Comprehensively Defines the Promoter-Position and Promoter-Sequence Determinants for Initial-Transcription Pausing. *Molecular cell*, **79**, 797–811.

44. Belogurov G., Vassilyeva M., Svetlov V., Klyuyev S., Grishin N., Vassilyev D., and Artsimovitch I. (2007). Structural basis for converting a general transcription factor into an operon-specific virulence regulator. *Mol. Biosyst*, **26**, 117–129.
45. Hudson B.P., Quispe J., Lara-Gonzalez S., Kim Y., Berman H.M., Arnold E., Ebright R.H., Lawson C.L. (2009) Three-dimensional EM structure of an intact activator-dependent transcription initiation complex. *Proc Natl Acad Sci USA*, **106**, 19830-19835.
46. Sambrook J., Russell D. (2001) Molecular cloning: A laboratory manual (Cold Spring harbour, NY, Cold Spring Haror Laboratory).
47. Niu W., Kim Y., Tau G., Heyduk T., Ebright R.H. (1996) Transcription activation at class II CAP-dependent promoters: two interactions between CAP and RNA polymerase. *Cell*, **87**, 1123-1134.
48. Mukhopadhyay J., Mekler V., Kortokhonjia E., Kapanidis A.N., Ebright Y.W., Ebright R.H. (2003) Fluorescence resonance energy transfer (FRET) in analysis of transcription-complex structure and function. *Methods Enzymol*, **371**, 144-159.
49. Dulin D., Bauer D.L.V., Malinen A.M., Bakermans J.J.W., Kaller M., Morichaud Z., Petushkov I., Depken M., Brodolin K., Kulbachinskiy A., Kapanidis A.N. (2018) Pausing controls branching between productive and non-productive pathways during initial transcription in bacteria. *Nat Commun.* Apr 16;1478.
50. Holden S., Uphoff S., Hohlbein J., Yadin D., Le Reste L., Britton O.J., Kapanidis A.N. (2010) Defining the limits of single-molecule FRET resolution in TIRF microscopy. *Biophys J*, **99**, 3102-3111.
51. Axelrod D., Thompson N.L., Burghardt T.P. (1983) Total internal inflection fluorescent microscopy. *J Microsc* **129**, 19-28.
52. Kapanidis A.N., Lee N.K., Laurence T.A., Doose S., Margeat E., Weiss S. (2004) Fluorescence-aided molecule sorting: analysis of structure and interactions by alternating-laser excitation of single molecules. *Proc Natl Acad Sci USA*, **101**, 8936-8941.
53. Lee N.K., Kapanidis A.N., Wang Y., Michalet X., Mukhopadhyay J., Ebright R.H., Weiss S. (2005) Accurate FRET measurements within single diffusing biomolecules using alternating-laser excitation. *Biophys J*, **88**, 2939-2953.
54. Van de Meent, J.W., Bronson J.E., Wiggins C.H., Gonzalez R.L. Jr. (2014) Empirical Bayes methods enable advanced population-level analyses of single-molecule FRET experiments. *Biophys J*, **106**, 1327-1337.

Figure Legends

Figure 1. smUIFE: DNA unwinding in the upstream part of the transcription bubble precedes DNA unwinding in the downstream part of the transcription bubble.

- A.** (*top*) Design of experiment monitoring promoter unwinding in real time. Grey, RNAP; orange, RNAP clamp; purple dot, RNAP active-center; black, ds-DNA; blue, ss-DNA; light green, Cy3 on ds-DNA; dark green, Cy3 on ss-DNA. (*bottom*) A cropped area ($0.94\ \mu\text{m} \times 1.034\ \mu\text{m}$) of the field of view, showing appearance and enhancement of fluorescence signal from binding of single Cy3-labelled promoter fragment to an immobilised RNAP molecule.
- B.** (*left*) Time-trajectories of intensity from Cy3 on downstream segment of promoter bubble. Black, raw intensity; dark blue, idealised intensity; Hidden Markov Model (HMM)-assigned states: no promoter (black bars), closed promoter (light yellow bars) and open promoter (green bars). Frame rates: 50-ms, top and middle; 200-ms, bottom. Laser powers: 0.60 mW, top and middle; 0.15 mW, bottom. (*right*) Dwell-time histograms of promoter state before unwinding, t_{UNWIND} .
- C.** (*left*) Time-trajectories of intensity from Cy3 on upstream segment of promoter bubble. Colors as in B. Frame rates: 50 ms. Laser powers: 0.6 mW. (*right*) Dwell-time histograms of promoter state before unwinding, t_{UNWIND} .
- D.** Table comparing unwinding times for different promoter constructs.

Figure 2. smUIFE in the presence of an inhibitor that prevents RNAP clamp opening: preventing RNAP clamp opening does not prevent DNA unwinding.

- A.** Design of promoter unwinding experiment in presence of Myxopyronin (Myx). Blue sphere, Myx; rest as in 1A.

B. (*left*) Time-trajectory of intensity from Cy3 on upstream (*top*) and downstream (*bottom*) segment of promoter bubble. Colors as in 1B. Frame rates: 50-ms. Laser powers: 0.60 mW. (*right*) Dwell-time histograms of promoter state before unwinding, t_{UNWIND} .

Figure 3. smFRET: DNA unwinding occurs without RNAP clamp opening and is followed by RNAP clamp locking.

A. Design of experiment monitoring clamp status in real time. Black, ds-DNA; orange, RNAP clamp; grey, rest of RNAP; purple dot, RNAP active-center; blue, ss-DNA; green, Cy3B; and red, Alexa647.

B. Representative time-trajectories of E^* for experiments with a lacCONS promoter fragment, showing HMM-assigned closed clamp state (orange), locked-clamp state (red) and interstate transition (dark-blue). Expected range of E^* values for an open clamp state is highlighted in light blue. Frame rate: 100-ms. Laser powers: 200 μW in red and 500 μW in green.

C. HMM-assigned histograms and Gaussian fits of E^* for full time-trajectories from experiments with a lacCONS promoter fragment.

D. Dwell-time histograms of time before transition to the locked-clamp state, t_{LOCK} , for experiments with a lacCONS promoter fragment.

E. Table showing mean E^* ; difference in E^* (ΔE^*) between closed-clamp or locked-clamp states and time to transition to a locked-clamp state after initial binding for the lacCONS and lacCONS-GC promoter fragments.

Figure 4. "Bind-unwind-load-and-lock" mechanism for the formation of RPo

Orange, closed clamp; red, locked clamp; grey, rest of RNAP; purple dot, RNAP active-center; black, ds-DNA; magenta, partly unwound bubble and blue, fully unwound bubble.

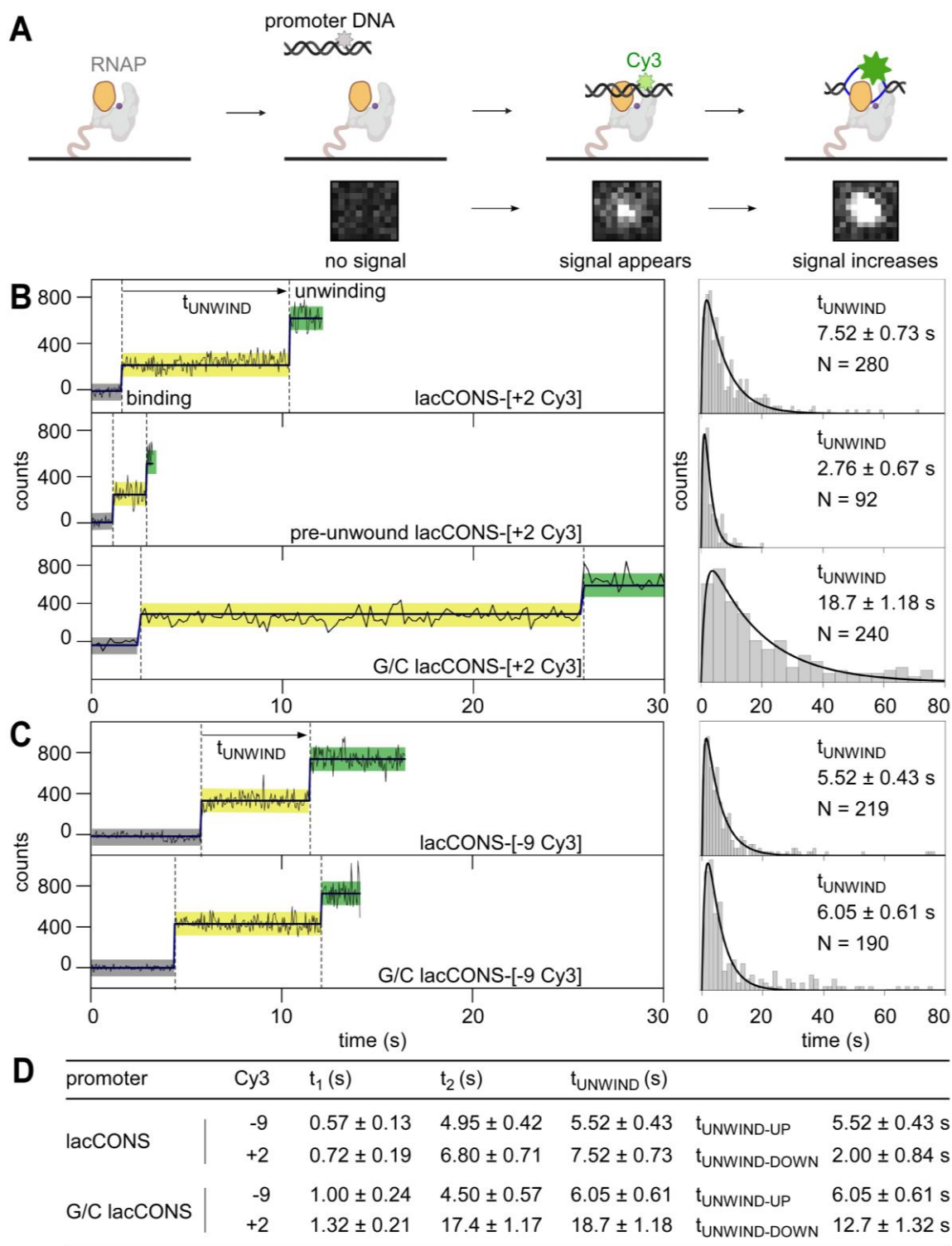


Figure 1. smUIFE: DNA unwinding in the upstream part of the transcription bubble precedes DNA unwinding in the downstream part of the transcription bubble.

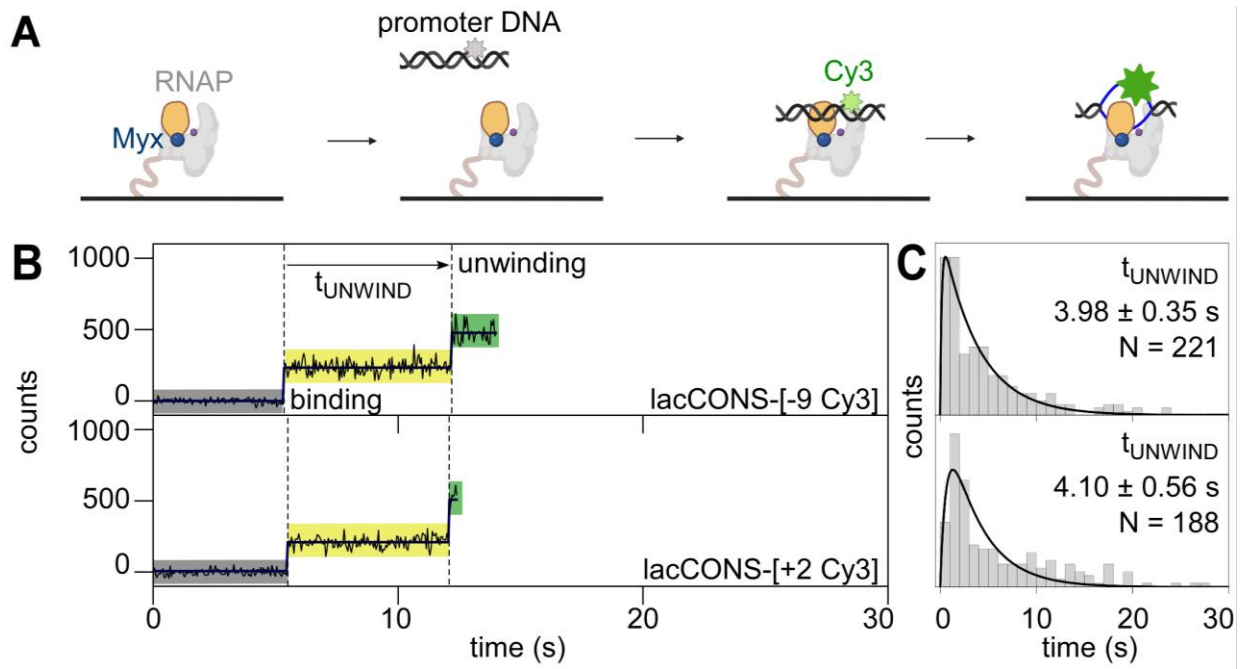


Figure 2. smUIFE in the presence of an inhibitor that prevents RNAP clamp opening: preventing RNAP clamp opening does not prevent DNA unwinding.

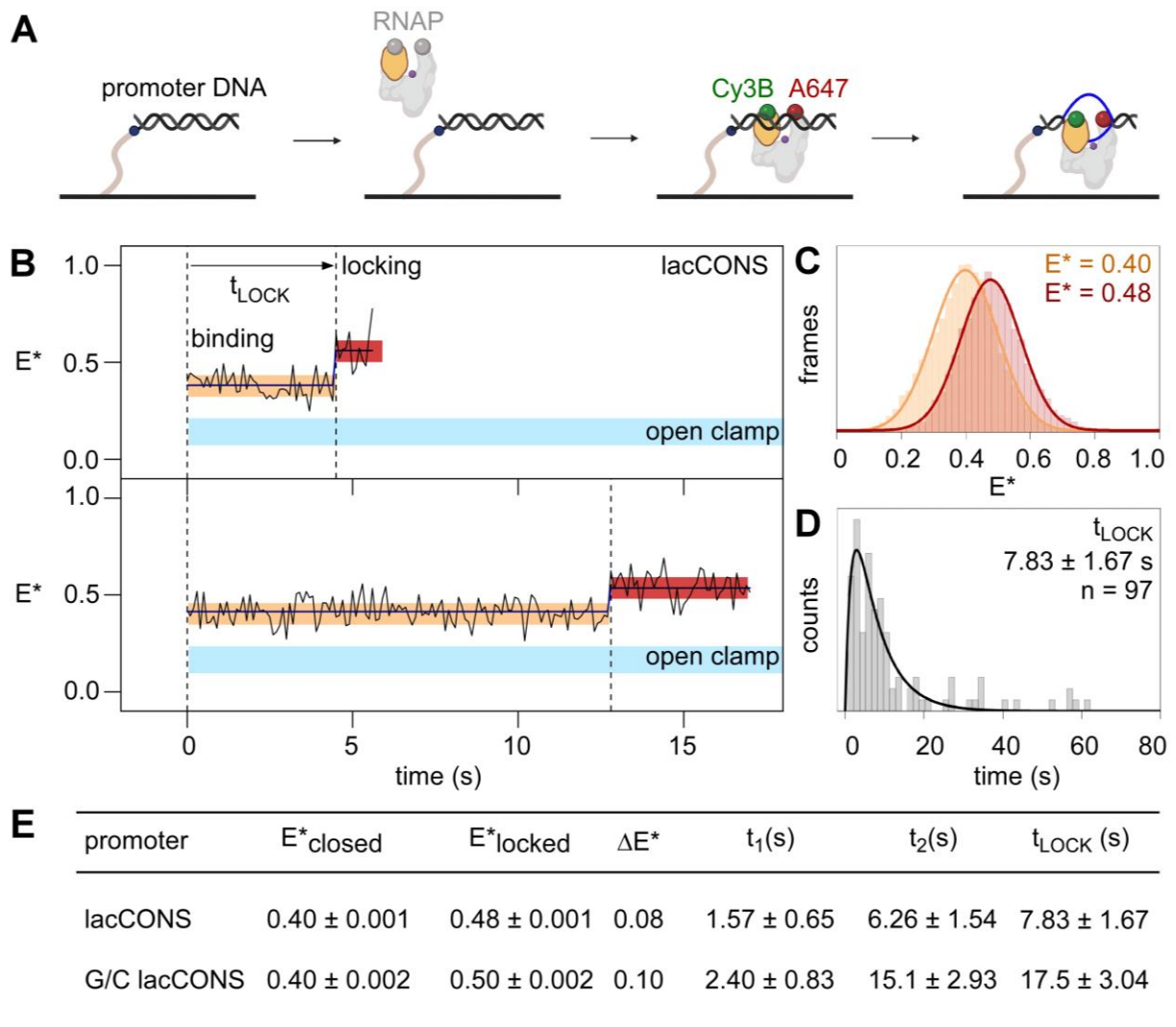


Figure 3. smFRET: DNA unwinding occurs without RNAP clamp opening and is followed by RNAP clamp locking.

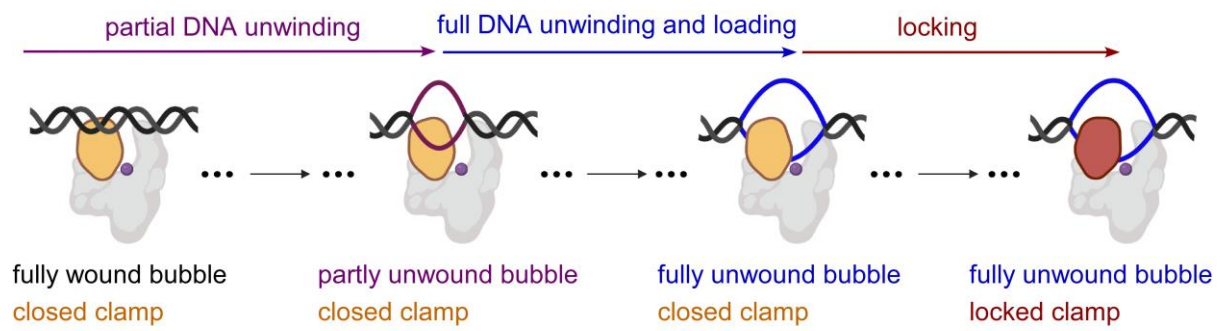


Figure 4. Bind-unwind-load-and-lock mechanism of formation of RPo.

Supplementary Figures

lacCONS-[+2-Cy3]:	<div> <div>-11</div> <div>+2</div> <div>5'-AGGCTTGACACTTTATGCTTCGGCTCGTATAATGTGTGGA</div> <div>T</div> <div>TTGTGAGAGCGGATAACAATTC-3'</div> </div> <div> <div>3'-TCCGAACGTGTGAAATACGAAGCCGAGCATATTACACACCTA</div> <div>A</div> <div>AACACTCTCGCCTATTGTTAAAG-5'</div> </div>
pre-unwound lacCONS-[+2-Cy3]:	<div> <div>5'-AGGCTTGACACTTTATGCTTCGGCTCGTATAATGTGTGGA</div> <div>T</div> <div>TTGTGAGAGCGGATAACAATTC-3'</div> </div> <div> <div>3'-TCCGAACGTGTGAAATACGAAGCCGAGCATCGGCACAACCTA</div> <div>A</div> <div>AACACTCTCGCCTATTGTTAAAG-5'</div> </div>
G/C lacCONS-[+2-Cy3]:	<div> <div>5'-AGGCTTGACACTTTATGCTTCGGCTCGTATAATGTGCGGC</div> <div>T</div> <div>TTGTGAGAGCGGATAACAATTC-3'</div> </div> <div> <div>3'-TCCGAACGTGTGAAATACGAAGCCGAGCATATTACACGCCG</div> <div>A</div> <div>AACACTCTCGCCTATTGTTAAAG-5'</div> </div>
lacCONS-[-9-Cy3]:	<div> <div>5'-AGGCTTGACACTTTATGCTTCGGCTCGTATAATGTGTGGAT</div> <div>T</div> <div>TTGTGAGAGCGGATAACAATTC-3'</div> </div> <div> <div>3'-TCCGAACGTGTGAAATACGAAGCCGAGCATAT</div> <div>T</div> <div>TACACACCTA</div> <div>A</div> <div>AACACTCTCGCCTATTGTTAAAG-5'</div> </div>
G/C lacCONS-[-9-Cy3]:	<div> <div>5'-AGGCTTGACACTTTATGCTTCGGCTCGTATAATGTGCGGCT</div> <div>T</div> <div>TTGTGAGAGCGGATAACAATTC-3'</div> </div> <div> <div>3'-TCCGAACGTGTGAAATACGAAGCCGAGCATAT</div> <div>T</div> <div>TACACGCCGA</div> <div>A</div> <div>AACACTCTCGCCTATTGTTAAAG-5'</div> </div>
biotin-lacCONS:	<div> <div>5'-biotin-AGGCTTGACACTTTATGCTTCGGCTCGTATAATGTGTGGAT</div> <div>T</div> <div>TTGTGAGAGCGGATAACAATTC-3'</div> </div> <div> <div>3'-TCCGAACGTGTGAAATACGAAGCCGAGCATATTACACACCTA</div> <div>A</div> <div>AACACTCTCGCCTATTGTTAAAG-5'</div> </div>
biotin-G/C lacCONS:	<div> <div>5'-biotin-AGGCTTGACACTTTATGCTTCGGCTCGTATAATGTGCGGCT</div> <div>T</div> <div>TTGTGAGAGCGGATAACAATTC-3'</div> </div> <div> <div>3'-TCCGAACGTGTGAAATACGAAGCCGAGCATATTACACGCCGA</div> <div>A</div> <div>AACACTCTCGCCTATTGTTAAAG-5'</div> </div>
biotin-non-promoter:	<div> <div>5'-biotin-AGGCGCTGTCCTTTATGCTTCGGCTCGCCGGTAGTGTGGAATTGTGAGAGCGGATAACAATTC-3'</div> </div> <div> <div>3'-TCCGCGACAGGAAATACGAAGCCGAGCGGCCATCACACCTTAACACTCTCGCCTATTGTTAAAG-5'</div> </div>
non-promoter-[Cy3]:	<div> <div>5'-AGGCGCTGTCCTTTATGCTTCGGCTCGCCGGTAGTGTGGA</div> <div>T</div> <div>TGTGAGAGCGGATAACAATTC-3'</div> </div> <div> <div>3'-TCCGCGACAGGAAATACGAAGCCGAGCGGCCATCACACCTTA</div> <div>A</div> <div>AACACTCTCGCCTATTGTTAAAG-5'</div> </div>

Figure 1-figure supplement 1. Sequence of consensus lac-promoter fragments used in the study.

Top strand: non-template DNA strand; bottom strand: template strand. Nucleotides labelled with Cy3 are shown in green. The numbering refers to the DNA position relative to the transcription start site.

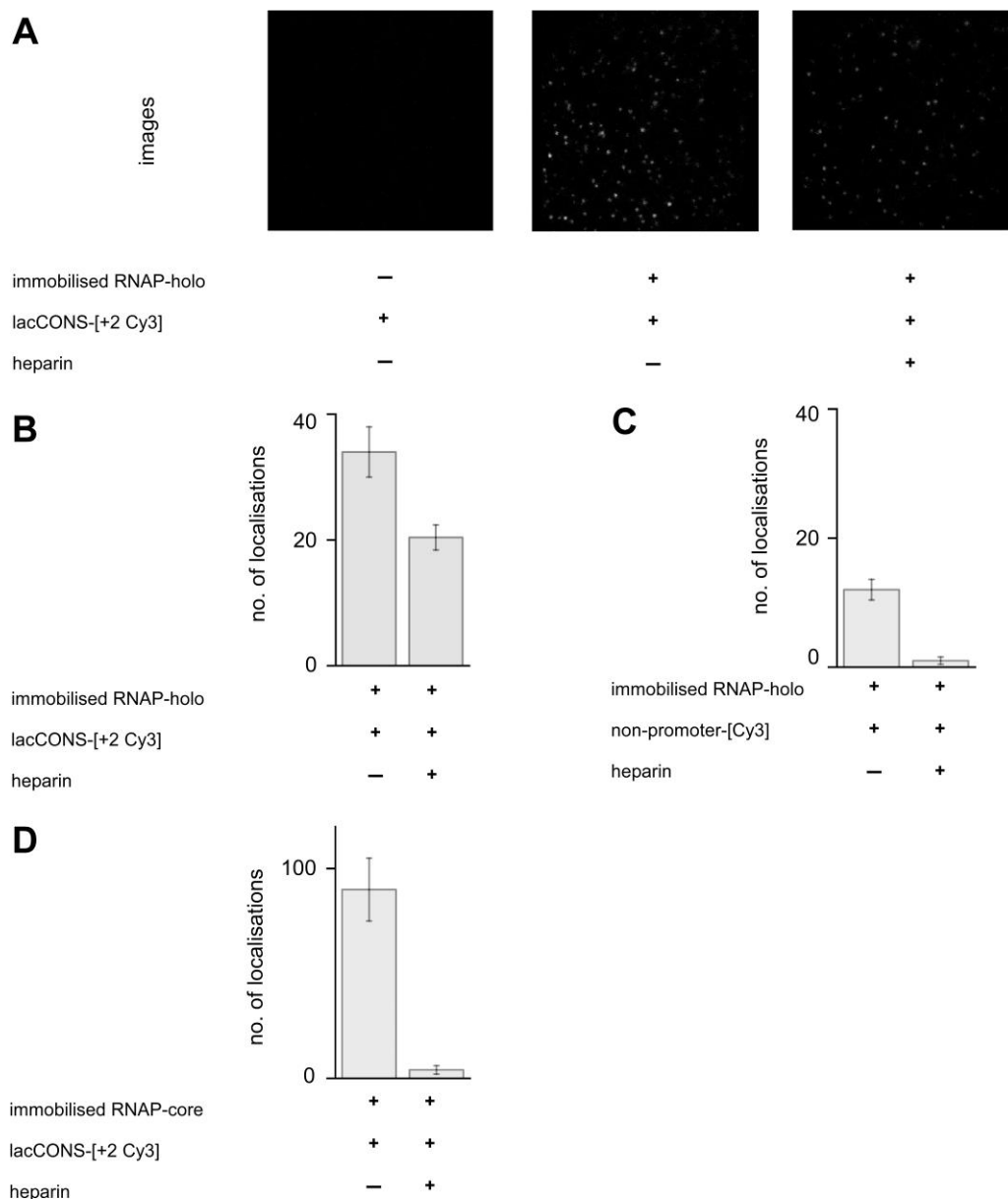


Figure 1-figure supplement 2. Characterisation of complexes between RNAP and Cy3-labelled DNA fragments.

- A.** Raw images (field of view: $24\ \mu\text{m} \times 24\ \mu\text{m}$) of immobilised hexahistidine-tagged RNAP holoenzyme (*left*), immobilised hexahistidine-tagged RNAP holoenzyme bound to lacCONS-[+2Cy3] promoter fragment before (*middle*), and after (*right*) addition of heparin.
- B.** Mean number of localisations per field of view for single lacCONS-[+2Cy3] promoter fragments bound to immobilised hexahistidine-tagged RNAP holoenzyme in absence and presence of heparin.
- C.** Mean number of localisations per field of view for single non-promoter-[Cy3] fragments bound to immobilised hexahistidine-tagged RNAP holoenzyme in absence and presence of heparin.
- D.** Mean number of localisations per field of view for single Cy3-labelled promoter fragments bound to immobilised hexahistidine-tagged RNAP core enzyme in absence and presence of heparin. Mean number of localisations are average of three measurements. Errors bars represent the standard deviation from the mean.

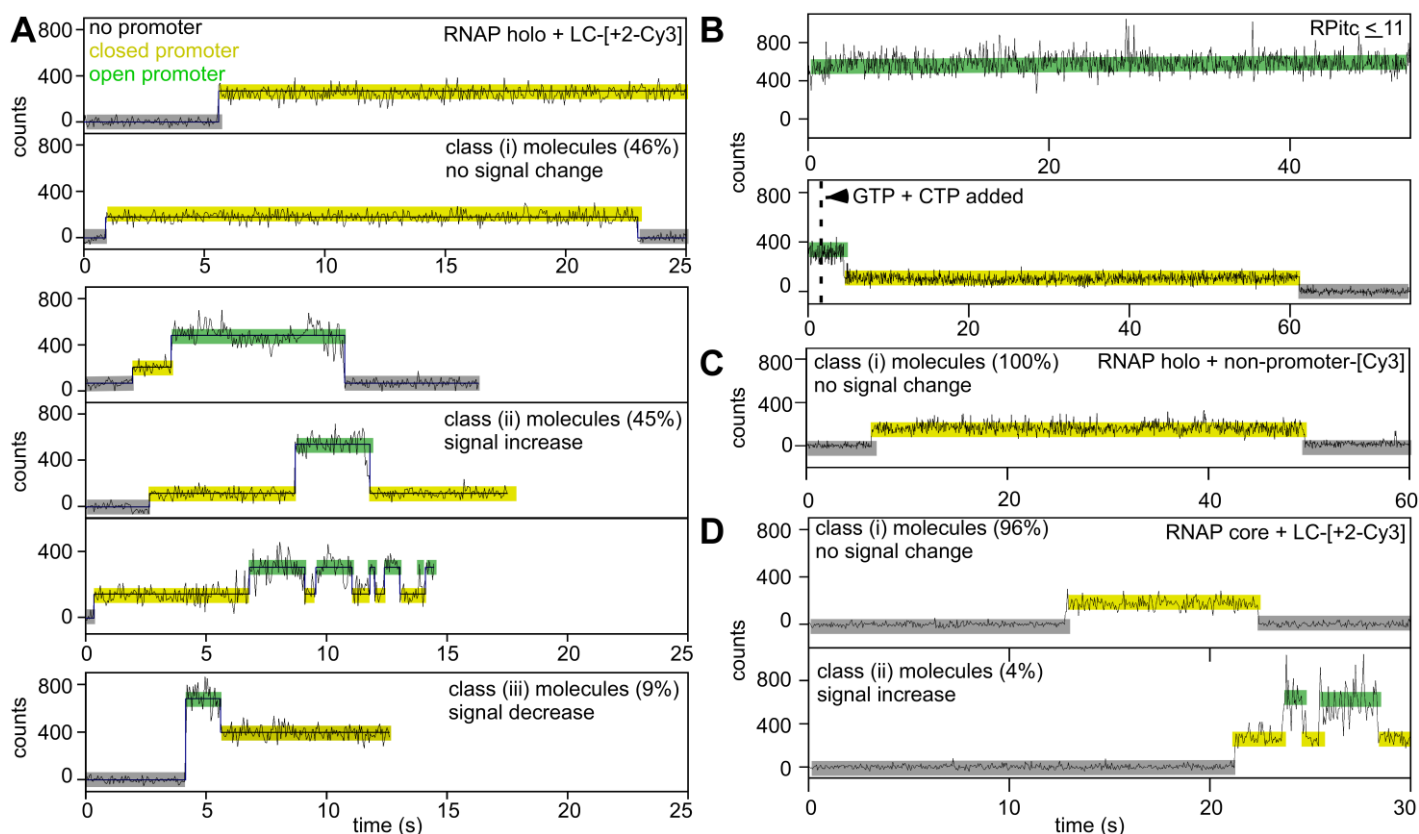
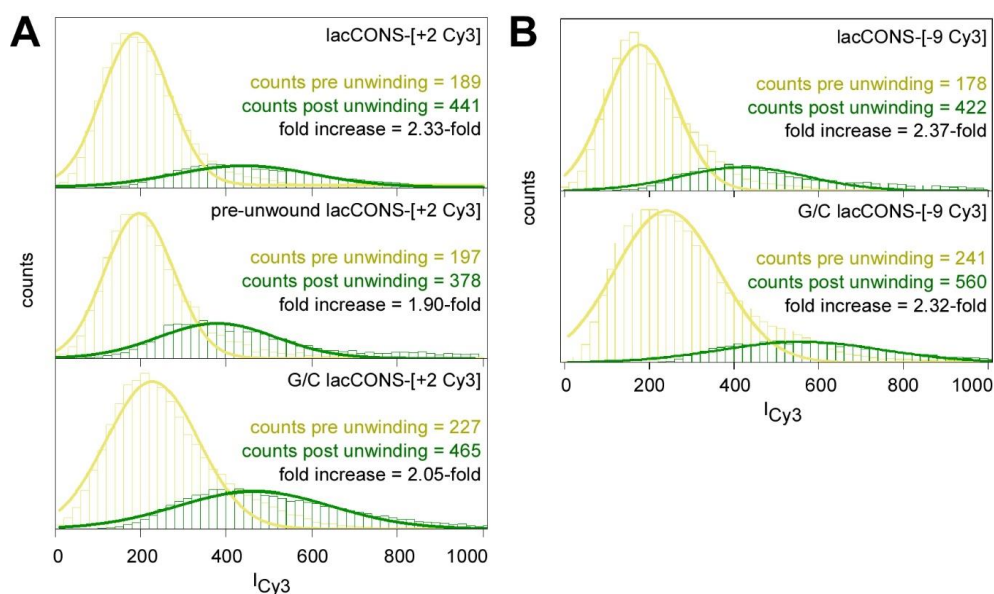


Figure 1-figure supplement 3. Representative intensity vs time trajectories from

- A.** Binding of lacCONS-[+2 Cy3] promoter fragment to immobilised RNAP holoenzyme.
- B.** (top) Stalled initial transcribing complexes ($RP_{itc} \leq 11$) formed with RNAP holoenzyme, lacCONS-[+2 Cy3] and subset of NTPs (ATP, GTP and UTP). (bottom) real time addition of NTPs (GTP and CTP) to stalled initial transcribing complexes ($RP_{itc} \leq 11$).
- C.** Binding of non-promoter-[Cy3] fragment to immobilised RNAP holoenzyme.
- D.** Binding of lacCONS-[+2 Cy3] promoter fragment to immobilised RNAP core enzyme. Black, raw intensity; dark blue, idealised intensity; Hidden Markov Model (HMM)-assigned states: no promoter (black bars), closed promoter (light yellow bars) and open promoter (green bars). Frame duration: 50-ms; Laser power: 0.60 mW.

953



954

955

956

957 **Figure 1-figure supplement 4. Fluorescence intensities from Cy3-labelled promoter fragments**
958 **pre- and post-unwinding.**

959 HMM-assigned histograms and Gaussian fits of fluorescence intensities, pre-unwinding (yellow) and
960 post-unwinding (green) for Cy3-labelled promoter fragments. Mean intensities for the two states and
961 fold-increase of intensities are shown (*inset*).

962 **A.** data for lacCONS-[+2Cy3] promoter fragments.

963 **B.** data for lacCONS-[-9Cy3] promoter fragments.

964

965

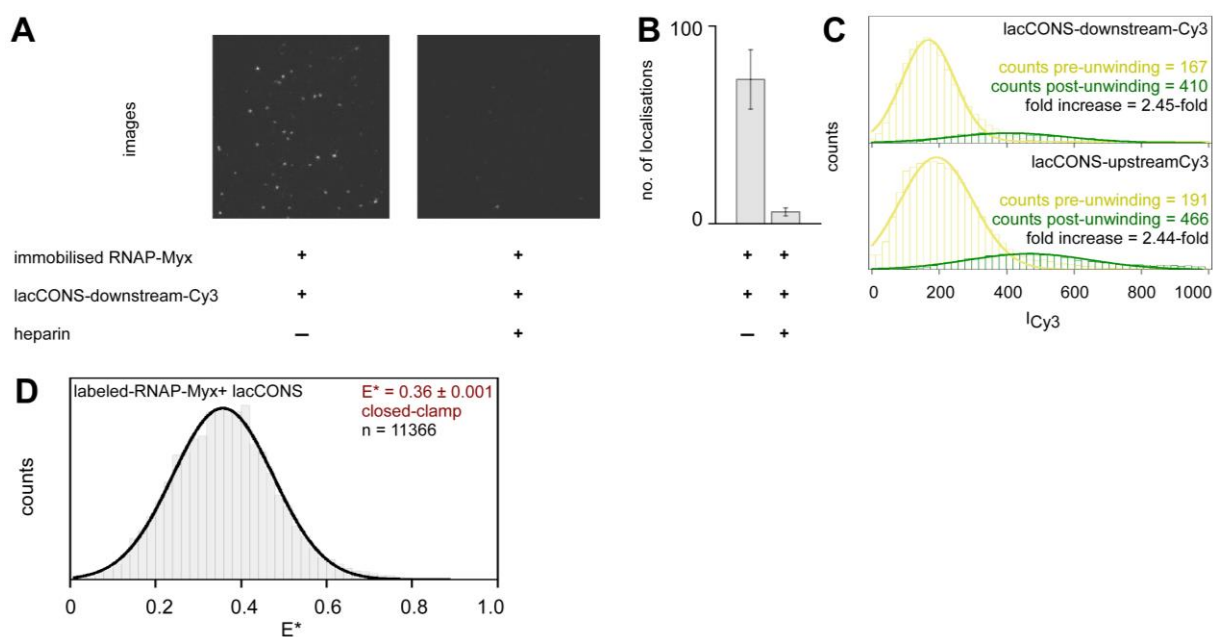
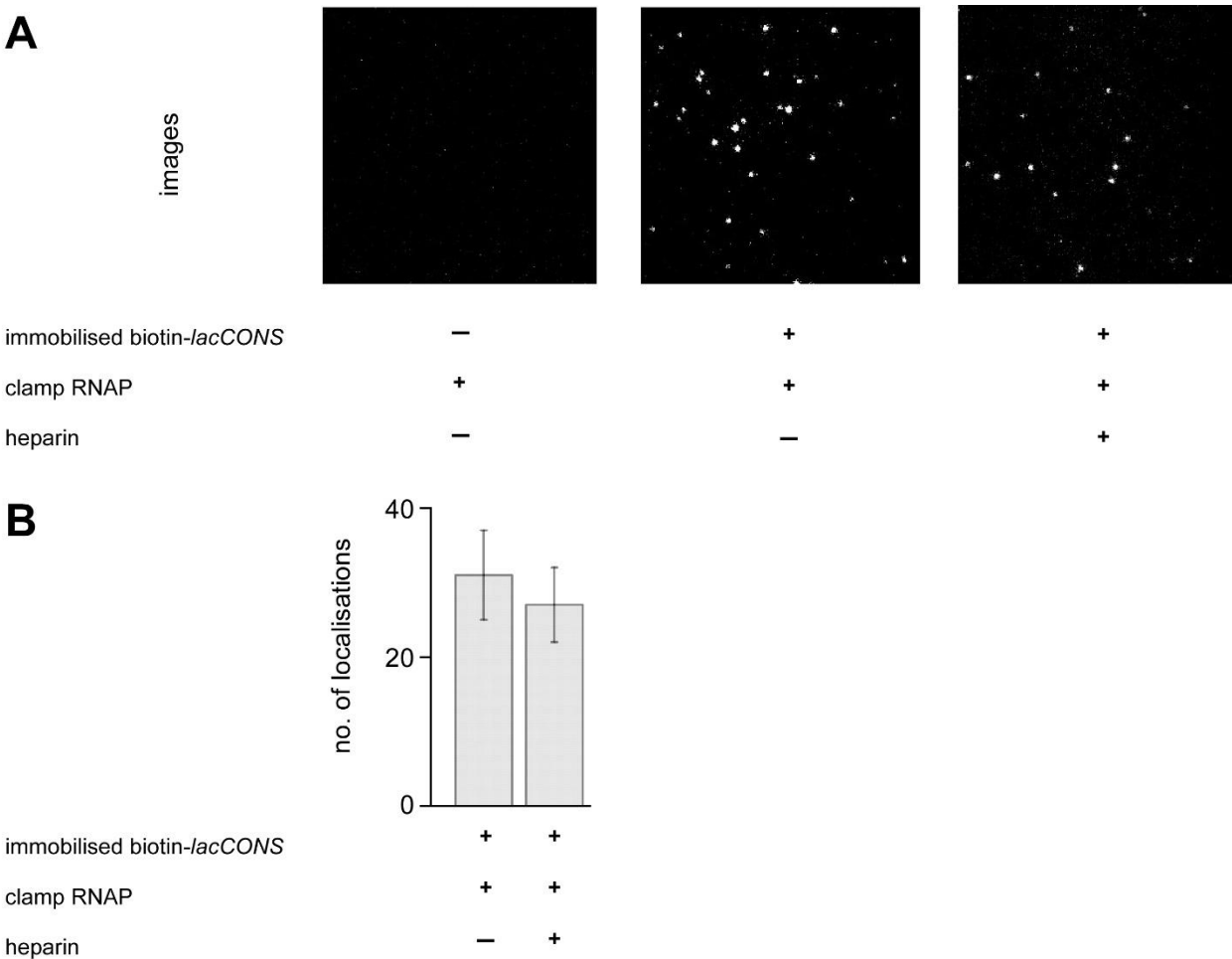


Figure 2-figure supplement 1. Characterisation of complexes formed between RNAP and promoter fragments in presence of Myxopyronin (Myx).

- A.** Raw images showing field of view ($24 \mu\text{m} \times 24 \mu\text{m}$) with immobilised biotin promoter fragment bound to labelled RNAP complexes formed in presence of Myxopyronin (Myx) (*left*), and with remaining immobilised hexahistidine-tagged RNAP holoenzyme complexes bound to Cy3-labelled promoter fragment, formed in presence of Myx, after addition of heparin (*right*).
- B.** Mean number of localisations per field of view for single Cy3-labelled promoter fragments bound to immobilised hexahistidine-tagged RNAP holoenzyme, formed in presence of Myx, before and after addition of heparin. Mean number of localisations are average of three measurements. Error bars represent the standard deviation from the mean.
- C.** HMM-assigned histograms and Gaussian fits of fluorescence intensities corresponding to pre-unwinding (yellow) and post-unwinding (green) states for promoter fragments with Cy3 on +2 position of the non-template strand (*top*) or -9 position of the template strand (*bottom*) of the promoter bubble. Mean intensities for the two states and fold-increase of intensities are shown (*inset*).
- D.** Histogram and Gaussian fit of E^* showing mean E^* values for clamp conformational state for clamp-labelled RNAP molecules bound to immobilised lacCONS-promoter fragments in presence of Myxopyronin.



989

990 **Figure 3-figure supplement 1. Characterisation of complexes formed between clamp-labelled**
991 **RNAP and immobilised promoter fragments.**

992 **A.** Raw images of the green emission channel showing field of view (24 mm × 24 mm) with
993 immobilised biotin-lacCONS promoter fragments (*left*), with immobilised biotin-lacCONS
994 promoter fragments bound to clamp-labelled RNAP (*middle*), and with remaining immobilised
995 biotin-lacCONS promoter fragments bound to clamp-labelled RNAP, after addition of heparin
996 (*right*).

997 **B.** Mean number of localisations per field of view for single clamp-labelled RNAP molecules with
998 both green (Cy3B) and red (Alexa647) probes, bound to immobilised biotin-lacCONS promoter
999 fragments, before and after addition of heparin. Mean number of localisations are average of three
1000 measurements. Error bars represent the standard deviation from the mean.

1001

1002

1003

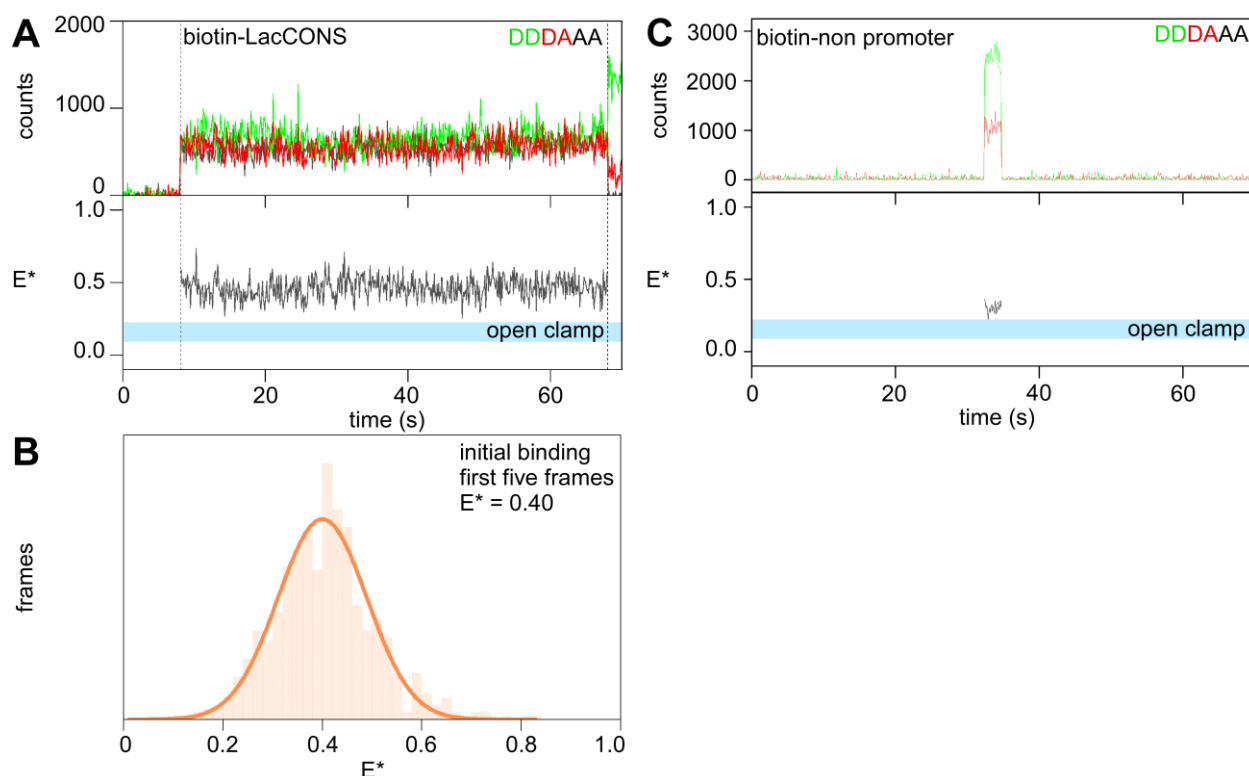


Figure 3-figure supplement 2. smFRET: initial binding of RNAP to surface immobilised promoter DNA fragments take place via a closed-clamp conformation.

- A.** Fluorescence intensity-vs-time trajectories showing simultaneous appearance (at ~8 s) of donor and acceptor signals from labelled-RNAP bound to biotin-lacCONS promoter fragment (*top*) and FRET efficiency, E^* (*bottom*). Range for expected E^* values corresponding to an open-clamp conformation is highlighted in cyan.
- B.** Histogram and Gaussian fit of E^* values for first five frames after binding define the mean E^* for initial binding. Frame duration: 100-ms. Laser powers: 200 μ W in red and 500 μ W in green.
- C.** Fluorescence intensity-vs-time trajectories showing simultaneous appearance of donor and acceptor signals from labelled-RNAP bound to biotin-non-promoter fragment (*top*) and FRET efficiency, E^* (*bottom*). Range for expected E^* values corresponding to an open-clamp conformation is highlighted in cyan.

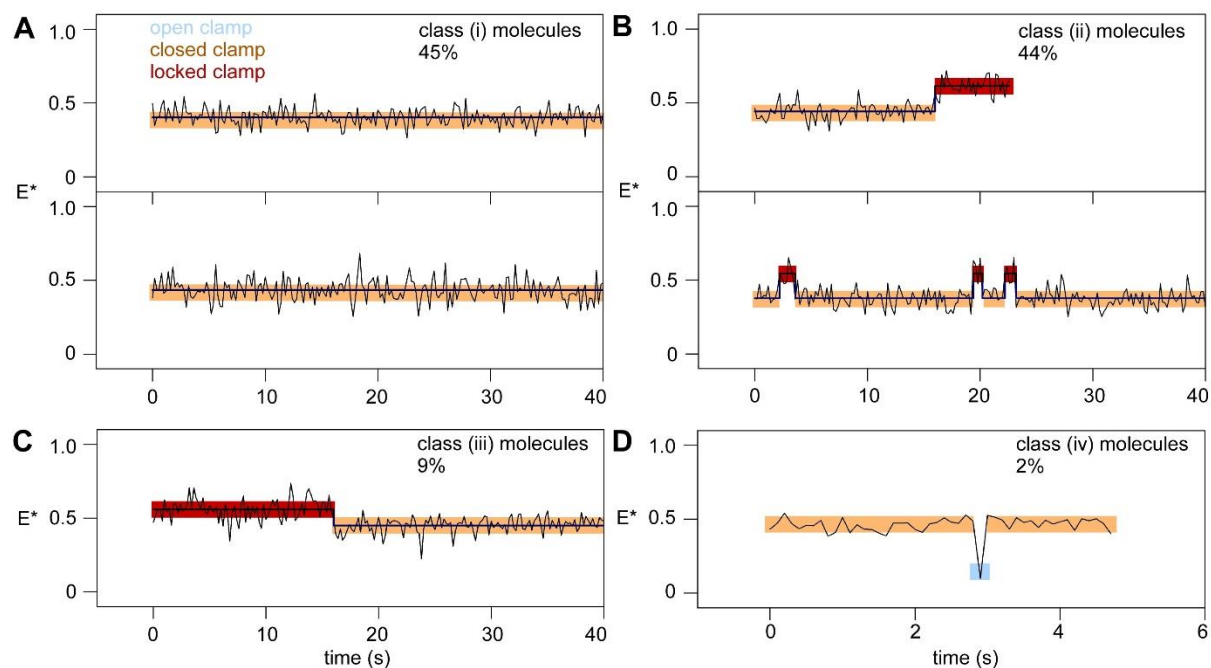


Figure 3-figure supplement 3. Classification for different time-trajectories of E^* of clamp labelled RNAP molecules bound to immobilised lacCONS-promoter fragments in real time.

HMM-assigned E^* time-trajectories showing closed-clamp states (orange), locked-clamp states (red), open-clamp states (cyan) and interstate transitions (dark-blue).

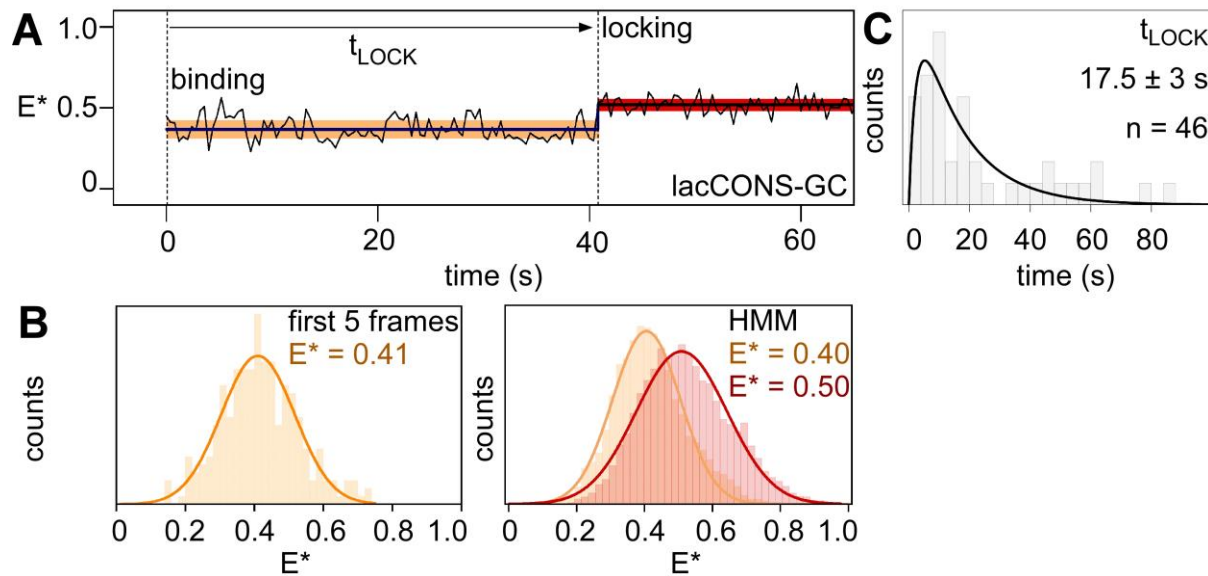


Figure 3-figure supplement 4. smFRET data showing binding of clamp-labelled RNAP to immobilised biotin-G/C lacCONS promoter fragments.

- A.** Time-trajectory of E^* , showing HMM-assigned closed-clamp state (orange) and locked-clamp state (red). Frame duration: 400-ms. Laser powers: 50 μ W in red and 150 μ W in green.
- B.** HMM-assigned histograms and Gaussian fits of E^* for first five-frames (*left*) and full time-trajectories (*right*).
- C.** Dwell-time histograms for time before transition to the locked-clamp state, t_{LOCK} .